A&A 610, A85 (2018)
https://doi.org/10.1051/0004-6361/201731730

Astronomy & Astrophysics

Precise weak lensing constraints from deep high-resolution K_s images: VLT/HAWK-I analysis of the super-massive galaxy cluster RCS2 $J232727.7-020437$ at $z = 0.70$⋆

Tim Schrabback[1], Mischa Schirmer[2], Remco F. J. van der Burg[3,4], Henk Hoekstra[5], Axel Buddendiek[1], Douglas Applegate[1,6], Maruša Bradač[7], Tim Eifler[8,9], Thomas Erben[1], Michael D. Gladders[10,6], Beatriz Hernández-Martín[1], Hendrik Hildebrandt[1], Austin Hoag[7], Dominik Klaes[1], Anja von der Linden[11], Danilo Marchesini[12], Adam Muzzin[13], Keren Sharon[14], and Mauro Stefanon[5]

[1] Argelander-Institut für Astronomie, Universität Bonn, Auf dem Hügel 71, 53121 Bonn, Germany
e-mail: schrabba@astro.uni-bonn.de
[2] Gemini Observatory, Southern Operations Center, Casilla 603, LaSerena, Chile
[3] IRFU, CEA, Université Paris-Saclay, 91191 Gif-sur-Yvette, France
[4] Université Paris Diderot, AIM, Sorbonne Paris Cité, CEA, CNRS, 91191 Gif-sur-Yvette, France
[5] Leiden Observatory, Leiden University, Niels Bohrweg 2, 2300 CA Leiden, The Netherlands
[6] Kavli Institute for Cosmological Physics, University of Chicago, 5640 South Ellis Avenue, Chicago, IL 60637, USA
[7] Department of Physics, University of California, Davis, CA 95616, USA
[8] Jet Propulsion Laboratory, California Institute of Technology, 4800 Oak Grove Dr., Pasadena, CA 91109, USA
[9] Center for Cosmology and Astro-Particle Physics, The Ohio State University, 191 W. Woodruff Ave, Columbus, OH 43210, USA
[10] Department of Astronomy and Astrophysics, University of Chicago, 5640 South Ellis Avenue, Chicago, IL 60637, USA
[11] Department of Physics and Astronomy, Stony Brook University, Stony Brook, NY 11794, USA
[12] Department of Physics and Astronomy, Tufts University, 574 Boston Avenue, Medford, MA 02155, USA
[13] Department of Physics and Astronomy, York University, 4700 Keele St., Toronto, Ontario MJ3 1P3, Canada
[14] Department of Astronomy, University of Michigan, 1085 S. University Ave, Ann Arbor, MI 48109, USA

Received 7 August 2017 / Accepted 26 October 2017

ABSTRACT

We demonstrate that deep good-seeing VLT/HAWK-I K_s images complemented with $g + z$-band photometry can yield a sensitivity for weak lensing studies of massive galaxy clusters at redshifts $0.7 \lesssim z \lesssim 1.1$, which is almost identical to the sensitivity of HST/ACS mosaics of single-orbit depth. Key reasons for this good performance are the excellent image quality frequently achievable for K_s imaging from the ground, a highly effective photometric selection of background galaxies, and a galaxy ellipticity dispersion that is noticeably lower than for optically observed high-redshift galaxy samples. Incorporating results from the 3D-HST and UltraVISTA surveys we also obtained a more accurate calibration of the source redshift distribution than previously achieved for similar optical weak lensing data sets. Here we studied the extremely massive galaxy cluster RCS2 $J232727.7-020437$ ($z = 0.699$), combining deep VLT/HAWK-I K_s images (point spread function with a $0\farcs35$ full width at half maximum) with LBT/LBC photometry. The resulting weak lensing mass reconstruction suggests that the cluster consists of a single overdensity, which is detected with a peak significance of 10.1σ. We constrained the cluster mass to $M_{200c}/(10^{15}\,M_\odot) = 2.06^{+0.28}_{-0.26}(\mathrm{stat.}) \pm 0.12(\mathrm{sys.})$ assuming a spherical Navarro, Frenk & White model and simulation-based priors on the concentration, making it one of the most massive galaxy clusters known in the $z \gtrsim 0.7$ Universe. We also cross-checked the HAWK-I measurements through an analysis of overlapping HST/ACS images, yielding fully consistent estimates of the lensing signal.

Key words. gravitational lensing: weak – galaxies: clusters: individual: RCS2 $J232727.7-020437$

1. Introduction

Light bundles from distant galaxies are distorted by the tidal gravitational field of foreground structures. These weak lensing distortions can be constrained statistically from the observed shapes of background galaxies, providing information about the differential projected mass distribution of the foreground objects, free of assumptions about their dynamical state (e.g. Bartelmann & Schneider 2001). To conduct such measurements, sufficiently unbiased estimates of galaxy shapes have to be obtained, corrected for the impact of the image point spread function (PSF). This is only possible if the observed galaxy images are sufficiently resolved, as the blurring PSF otherwise erases the shape information. Weak lensing observations therefore benefit from good image quality, which boosts the number density of sufficiently resolved galaxies and thus the signal-to-noise ratio, while simultaneously reducing the required level of PSF corrections and therefore systematic uncertainties (e.g. Massey et al. 2013).

For studies targeting more distant lenses it is vital to employ deep observations with superb image quality to measure the

⋆ Based on observations conducted with the ESO Very Large Telescope, the Large Binocular Telescope, and the NASA/ESA *Hubble* Space Telescope, as detailed in the acknowledgements.

shapes of the typically faint and small distant background galaxies carrying the signal. In red optical filters, queue-scheduled ground-based observations from the best sites achieve a stellar PSF full width at half maximum (FWHM*) $\simeq$0.″6–0.″7 in good conditions (e.g. Kuijken et al. 2015; Mandelbaum et al. 2018), which provides a good weak lensing sensitivity out to lens redshifts $z \sim 0.6$ in the case of deep integrations. Much higher resolution ($FWHM^* \simeq 0.''10$) can be achieved with the *Hubble* Space Telescope (HST), which has been used to probe the weak lensing signatures out to significantly higher redshifts when targeting galaxies (Leauthaud et al. 2012), galaxy clusters (e.g. Jee et al. 2011; Schrabback et al. 2018, S18 henceforth), or the statistical properties of the large-scale structure itself (Massey et al. 2007; Schrabback et al. 2010). However, HST has a relatively small field of view of $3.'3 \times 3.'3$ for its ACS/WFC detector, raising the need for time-consuming mosaics in order to cover a wider area on the sky. In particular, studies that aim to obtain accurate weak lensing mass measurements for massive galaxy clusters at moderately high redshifts ($0.7 \lesssim z \lesssim 1.1$) have so far required mosaic ACS images to probe the lensing signal out to approximately the cluster virial radius (e.g. S18; Jee et al. 2009; Thölken et al. 2018).

In this paper we demonstrate that deep ground-based imaging obtained in the HAWK-I K_s filter ($1.98\,\mu\text{m} \lesssim \lambda \lesssim 2.30\,\mu\text{m}$) under good seeing conditions can provide a viable alternative to mosaic HST observations for moderately deep weak lensing measurements. The observational set-up we describe provides several advantages for weak lensing studies. First, for an 8 m class telescope and typical conditions, the measured atmospheric PSF FWHM is reduced by $\simeq$40% at such long wavelengths compared to the V band (Martinez et al. 2010). As a result, delivered image qualities of $FWHM^* \simeq 0.''3$–$0.''4$ are achieved in K_s in good conditions without having to request the very best seeing quantile. While not quite reaching an HST-like resolution, this still provides a major advantage for weak lensing measurements compared to optical seeing-limited observations. The second advantage is the efficiency of selecting distant background sources in K (or K_s)-detected galaxy samples, using the "BzK selection" technique (Daddi et al. 2004) with observations taken in only three bands. As a third advantage, excellent deep reference samples selected in the near-infrared (NIR) have recently become available to infer the redshift distribution of the weak lensing source galaxies, including photometric redshifts from UltraVISTA (McCracken et al. 2012; Muzzin et al. 2013, and in prep.) and HST slitless spectroscopy from the 3D-HST programme (Momcheva et al. 2016). Finally, at $z \sim 2$ K_s imaging probes the light distribution of the smoother stellar component exhibiting lower shape noise, an advantage over optical imaging, which mostly maps the clumpy distribution of star forming regions seen at rest-frame UV wavelengths.

In this study we analyse new deep VLT/HAWK-I K_s observations of the galaxy cluster RCS2 J232727.7−020437 (hereafter: RCS2 J2327; $z = 0.699$, Sharon et al. 2015) discovered in the Second Red-Sequence Cluster Survey (RCS2; Gilbank et al. 2011). Optical, Sunyaev-Zel'dovich, X-ray, dynamical, strong lensing, and initial weak lensing measurements of the cluster are consistent with an extremely high mass of $M_{200c} \simeq 2$–$3 \times 10^{15}\,M_\odot$ (Menanteau et al. 2013; Sharon et al. 2015; Buddendiek et al. 2015; Hoag et al. 2015), where $M_{\Delta c}$ indicates the mass within the sphere containing an average density that exceeds the critical density of the Universe at the cluster redshift by a factor Δ. Hence, this is one of the most massive clusters known at a comparable or higher redshift.

King et al. (2002) presented the first and previously only weak lensing analysis based on shape measurements in K_s images. Their analysis targeting a massive low-redshift cluster is based on imaging obtained with SofI on the 3.6 m ESO-NTT with an image resolution of 0.″73. Our analysis exploits much deeper K_s imaging with a resolution that is better by a factor two, as needed for high-redshift weak lensing constraints. We explicitly compare the weak lensing performance achieved with these new K_s data to the weak lensing analysis of galaxy clusters at similar redshift from S18. These authors employed 2×2 HST/ACS mosaics of single-orbit depth taken in the $F606W$ filter for shape measurements, and a photometric source selection based on $V_{606} - I_{814}$ colour to remove cluster galaxies and preferentially select distant background galaxies.

This paper is organised as follows: We summarise relevant weak lensing theory and notation in Sect. 2. Section 3 describes the analysed data sets and data reduction. Section 4 provides details on the shape and colour measurements, the background selection, an estimation of the source redshift distribution, an analysis of the galaxy ellipticity dispersion, and a comparison to shear estimates from HST measurements. Section 5 presents the cluster mass reconstruction, the derived cluster mass constraints, and the comparison to previous studies of the cluster. We compare the weak lensing performance of the HAWK-I data and the previously employed ACS mosaics in Sect. 6 and conclude in Sect. 7.

Throughout this paper we assume a flat ΛCDM cosmology characterised through $\Omega_m = 0.3$, $\Omega_\Lambda = 0.7$, $H_0 = 70\,h_{70}\,\text{km}\,\text{s}^{-1}$ and $h_{70} = 1$, as approximately consistent with recent constraints from the cosmic microwave background (e.g. Hinshaw et al. 2013; Planck Collaboration XIII 2016), unless explicitly stated otherwise. At the cluster redshift of $z = 0.699$, 1″ on the sky corresponds to a physical separation of 7.141 kpc in this cosmology. All magnitudes are in the AB system.

2. Summary of relevant weak lensing theory

In the weak lensing regime, the gravitational lensing effect of a lens at redshift z_l (assumed to be fixed here) onto the shape of a background galaxy at redshift z_s and an observed position $\boldsymbol{\theta}$ can be described through the anisotropic reduced shear

$$g(\boldsymbol{\theta}, z_s) = \frac{\gamma(\boldsymbol{\theta}, z_s)}{1 - \kappa(\boldsymbol{\theta}, z_s)}\,, \tag{1}$$

which is a rescaled version of the unobservable shear $\gamma(\boldsymbol{\theta}, z_s)$, and the isotropic convergence

$$\kappa(\boldsymbol{\theta}, z_s) = \Sigma(\boldsymbol{\theta})/\Sigma_{\text{crit}}(z_l, z_s), \tag{2}$$

(see e.g. Bartelmann & Schneider 2001 for a general review and Hoekstra et al. 2013 for applications to clusters). The latter is defined as the ratio of the surface mass density $\Sigma(\boldsymbol{\theta})$ and the critical surface mass density

$$\Sigma_{\text{crit}}(z_l, z_s) = \frac{c^2}{4\pi G}\frac{1}{D_l(z_l)\beta(z_l, z_s)}, \tag{3}$$

where c and G are the speed of light and the gravitational constant, respectively, while D_l denotes the angular diameter distance to the lens. The geometric lensing efficiency

$$\beta(z_l, z_s) = \max\left[0, \frac{D_{ls}(z_l, z_s)}{D_s(z_s)}\right], \tag{4}$$

is defined in terms of the angular diameter distances from the observer to the source D_s, and from the lens to the source D_{ls}.

Given that they are both computed from second-order derivatives of the lensing potential, the weak lensing shear γ and convergence κ are linked. The spatial distribution of the convergence can therefore be reconstructed from the shear field up to an integration constant (Kaiser & Squires 1993), which represents the mass-sheet degeneracy (Schneider & Seitz 1995).

Weak lensing shape measurement algorithms aim to obtain unbiased estimates of the complex galaxy ellipticity

$$\epsilon = \epsilon_1 + \mathrm{i}\epsilon_2 = |\epsilon| \mathrm{e}^{2\mathrm{i}\varphi} . \tag{5}$$

In the idealised case of an object that has concentric elliptical isophotes with a constant position angle φ and constant ratios of the semi-major and semi-minor axes a and b, these are related to the ellipticity as $|\epsilon| = (a-b)/(a+b)$. The ellipticity transforms under weak reduced shears ($|g| \ll 1$) as

$$\epsilon \simeq \epsilon_s + g, \tag{6}$$

(for the general case see Seitz & Schneider 1997; Bartelmann & Schneider 2001). The intrinsic source ellipticity ϵ_s is expected to have a random orientation, yielding an expectation value $\langle \epsilon_s \rangle = 0$. Hence, ellipticity measurements provide noisy estimates for the local reduced shear, where the noise level is given by the dispersion

$$\sigma_\epsilon = \sigma(\epsilon - g) \simeq \sqrt{\sigma_{\mathrm{int}}^2 + \sigma_{\mathrm{m}}^2} , \tag{7}$$

which has contributions from both the intrinsic ellipticity dispersion $\sigma_{\mathrm{int}} = \sigma(\epsilon_s)$ of the galaxy sample[1] and measurement noise σ_{m} (e.g. Leauthaud et al. 2007; S18). Assuming dominant shape noise, the signal-to-noise ratio of the detection of the weak lensing reduced shear signal scales as

$$\left(\frac{S}{N}\right)_{\mathrm{WL}} \propto f \equiv \frac{\sqrt{n_{\mathrm{gal}}}\langle\beta\rangle}{\sigma_{\epsilon,\mathrm{eff}}} , \tag{8}$$

where n_{gal} indicates the weak lensing source density on the sky and $\sigma_{\epsilon,\mathrm{eff}}$ corresponds to the effective value of σ_ϵ computed taking possible shape weights into account. The weak lensing signal-to-noise ratio also depends on the mass, mass distribution, and radial fitting range (e.g. Bartelmann & Schneider 2001). Shape weights w_i also need to be taken into account when computing $\langle\beta\rangle$, where we employ magnitude-dependent weights

$$w_i(\mathrm{mag}_i) = \sigma_\epsilon^{-2}(\mathrm{mag}_i), \tag{9}$$

which are directly related to the expected noise in the reduced shear estimate for galaxy i. In this case the effective ellipticity dispersion for the sample from Eq. (8) becomes

$$\sigma_{\epsilon,\mathrm{eff}} = \left(N^{-1} \sum_{i=1}^{N} w_i \right)^{-\frac{1}{2}} . \tag{10}$$

For cluster weak lensing analyses it is useful to decompose the ellipticity (and likewise the reduced shear) into a tangential component carrying the signal

$$\epsilon_t = -\epsilon_1 \cos 2\phi - \epsilon_2 \sin 2\phi, \tag{11}$$

[1] We absorb the effective broadening of the observed ellipticity distribution due to cosmological weak lensing by uncorrelated large-scale structure in σ_{int}. In Eq. (7) g refers to the reduced shear caused by the targeted cluster.

where ϕ denotes the azimuthal angle with respect to the cluster centre and the 45 degrees-rotated cross-component

$$\epsilon_\times = +\epsilon_1 \sin 2\phi - \epsilon_2 \cos 2\phi. \tag{12}$$

The averaged tangential ellipticity profile provides an estimate for the tangential reduced shear profile $g_t(r)$ of the cluster, which we fit using model predictions from Wright & Brainerd (2000) that assume a spherical NFW density profile (Navarro et al. 1997).

3. Data and data reduction

In our analysis we make use of high-resolution VLT/HAWK-I K_s images for the weak lensing shape measurements, which we complement with LBT/LBC imaging for a colour selection. We additionally analyse overlapping HST/ACS data to cross-check the VLT/HAWK-I weak lensing constraints.

3.1. VLT/HAWK-I data

RCS2 J2327 was observed with VLT UT4 using HAWK-I under programme 087.A-0933 (PI: Schrabback). HAWK-I is a high-throughput NIR imager equipped with a 2×2 mosaic of 2048×2048 Rockwell HgCdTe MBE HAWAII 2 RG arrays, with a plate scale of $0\farcs106$ pixel^{-1} and a $7\farcm5 \times 7\farcm5$ field of view (see Kissler-Patig et al. 2008, for details). Here we analyse K_s band images observed using large dither steps to cover the $\sim 15''$ gaps between the detectors. In total, 326×80 s exposures were obtained (total exposure time 7.2 h), some of which were repetitions because the seeing constraint (K_s band image quality $\leq 0\farcs4$) was not fulfilled. Each 80 s exposure was constructed from 8×10 s internal sub-exposures to avoid background saturation, averaged using on-detector arithmetics.

The data were reduced using `THELI` (Erben et al. 2005; Schirmer 2013) following standard procedures, including dark subtraction and flat fielding. A dynamic two-pass background subtraction including object masking was employed to remove the sky background from individual exposures. The background models were calculated from a floating median of the eight closest images in time, corresponding to a time window of 13–15 min. An accurate astrometric reference catalogue is required to align the images on sky. The 2MASS catalogue has insufficient source density for this purpose, as RCS2 J2327 is located at high galactic latitude of $-58°$. Thus, we first processed and co-added CFHT Megaprime i-band data (PI: H. Hoekstra), for which an astrometric calibration was possible using 2MASS thanks to the larger field of view. We then extracted a deep astrometric reference catalogue from the CFHT data, which was used both for the HAWK-I reduction and the reductions described in Sects. 3.2 and 3.3. The astrometry for the HAWK-I data was determined by `THELI` via `Scamp` (Bertin 2006). The relative positions of the detectors were accurately fixed using the dithered exposures and a fixed third-order distortion polynomial was used to describe the non-linear terms. In total, relative image registration is accurate to $\sim$1/10th of a pixel, which is well sufficient for our shear analysis. Image co-addition and resampling in `THELI` was performed with `SWarp` (Bertin et al. 2002), using a Lanczos3 kernel matched to the well-sampled PSF.

Given the variation in seeing we created two separate stacks. The first stack is generated from all exposures for photometric measurements, yielding a total integration time of 26.1 ks and a median stellar $FWHM^* = 0\farcs40$ as measured by `SExtractor` (Bertin & Arnouts 1996). The second stack is used for the

shape measurements. Here we exclude exposures with poorer image quality, yielding a shorter total integration time of 17.1 ks (4.8 h, or ∼7 h including overheads), but a better image quality with a median $FWHM^* = 0\farcs35$. To simplify the comparison to the weak lensing literature we also report the median stellar FLUX_RADIUS parameter from `SExtractor` $r_f^* = 0\farcs22$ and the median stellar half-light radius from `analyseldac` (Erben et al. 2001) $r_h^* = 0\farcs19$.

3.2. LBT/LBC data

RCS2 *J*2327 was also observed by the Large Binocular Telescope (LBT) on Oct. 02, 2010 (PI: Eifler) under good seeing conditions (≃0.″7), where we make use of *g*-band observations obtained with LBC_BLUE (Giallongo et al. 2008) and *z*-band observations obtained with LBC_RED. The data were reduced using `THELI` following standard procedures, yielding co-added total integration times of 2.4 ks in the *g* band and 3.0 ks in the *z* band.

3.3. HST/ACS data

To cross-check our HAWK-I shape measurements we also reduced and analysed HST/ACS observations (HST-GO 13177, PI: Bradač) of RCS2 *J*2327 conducted with the *F*814*W* filter as part of the *Spitzer* Ultra Faint SUrvey Program (Bradač et al. 2014). This includes a central pointing (integration time 5.6 ks) and four parallel fields (integration times 3.6–5.5 ks) that overlap with the outskirts of our HAWK-I observations. In order to generate a colour image we also processed central ACS observations conduced in the *F*435*W* filter (integration time 4.2 ks) as part of the HST-GO programme 10846 (PI: Gladders).

Following S18 we reduced these data employing the pixel-level correction for charge-transfer inefficiency from Massey et al. (2014), the standard ACS calibration pipeline `CALACS` for further basic reduction steps, `MultiDrizzle` (Koekemoer et al. 2003) for the cosmic ray removal and stacking[2], and scripts from Schrabback et al. (2010) for the image registration and optimisation of masks and weights.

4. Analysis

4.1. HAWK-I shape measurements

We detected objects with `SExtractor` and measure weak lensing shapes using the `analyseldac` (Erben et al. 2001) implementation of the KSB+ formalism (Kaiser et al. 1995; Luppino & Kaiser 1997; Hoekstra et al. 1998) as detailed in Schrabback et al. (2007), employing the correction for multiplicative noise bias as a function of the `analyseldac` signal-to-noise ratio from Schrabback et al. (2010). Analysing the measured shapes of stellar images in our K_s best-seeing stack we find that the HAWK-I PSF is well behaved in the majority of the field of view with PSF polarisation amplitudes $|e^*| \lesssim 0.05$, where

$$e = e_1 + \mathrm{i}e_2 = \frac{Q_{11} - Q_{22} + 2\mathrm{i}Q_{12}}{Q_{11} + Q_{22}}\,, \tag{13}$$

is defined via weighted second-order brightness moments Q_{ij} as detailed in Schrabback et al. (2007). However, the PSF degrades noticeably towards lower *y* positions with larger stellar polarisations and half-light radii r_h^* as computed by `analyseldac` (see Fig. 1). We find that the spatial variations of the KSB+ PSF parameters can be interpolated well using third-order polynomials combining stars from all chips. For the weak lensing analysis we required galaxies to be sufficiently resolved with half-light radii $r_h > 1.2 r^*_{h,\mathrm{mod}}(x,y)$, where $r^*_{h,\mathrm{mod}}(x,y)$ indicates the polynomial interpolation of the measured stellar half-light radii at the position of the galaxy. We selected galaxies with a flux signal-to-noise ratio defined via the auto flux from `SExtractor` of $(S/N)_{\mathrm{flux}} = \mathrm{FLUX\_AUTO/FLUXERR\_AUTO} > 10$. Shape selections were also applied according to the trace of the "pre-seeing" shear polarisability tensor $\mathrm{Tr}\,P^g/2 > 0.1$ and PSF-corrected ellipticity estimate $|\epsilon| < 1.4$. We masked regions around bright foreground objects and reject galaxies that are flagged by `SExtractor` or `analyseldac`, for example owing to the presence of a nearby object. Prior to the photometric background selection our catalogue of galaxies with weak lensing shape estimates has a source number density of 45 arcmin^{-2}.

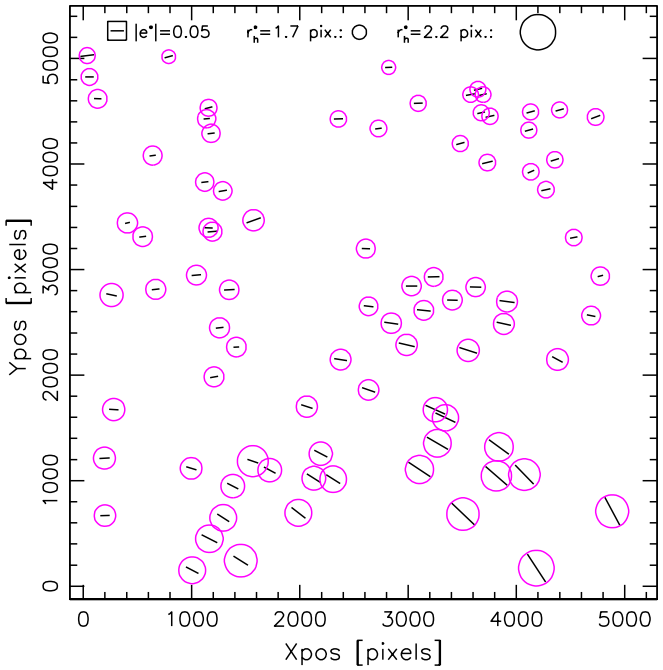

Fig. 1. Spatial variation of the PSF in our best-seeing stack of the HAWK-I K_s observations of RCS2 *J*2327: each whisker indicates the measured polarisation e^* of a star, while the circle indicates its half-light radius r_h^* from `analyseldac` (see the reference whisker and circles at the top for the absolute scale). In this stack north is up and east is left, matching the orientation of the input frames (observations obtained with a default 0° position angle).

Analysing ACS-like image simulations containing weak simulated shears ($|g| < 0.06$), Schrabback et al. (2010) estimated that the basic shape measurement algorithm also employed in this work leads to residual multiplicative shear biases $|m| < 2\%$. However, these authors neither tested the performance in the stronger shear regime of clusters nor the sensitivity to the assumed input ellipticity distribution of galaxies, which can affect measured noise biases (Viola et al. 2014; Hoekstra et al. 2015). We therefore conducted additional tests with new simulations created with `galsim` (Rowe et al. 2015). The details of these tests will be described in Hernández-Martín et al. (in prep.). For our current work, the most relevant result from these simulations is that multiplicative biases are limited to $|m| \lesssim 3\%$

[2] We used the `lanczos3` kernel with the native pixel scale 0.″05 and a `pixfrac` of 1.0. These settings minimise the impact of noise correlations while introducing only a low level of aliasing for the ellipticity measurements (Jee et al. 2007).

for reduced shears $|g| < 0.2$ and variations in the intrinsic ellipticity dispersion in the range $0.2 \leq \sigma_{\rm int} \leq 0.3$. For stronger shear $|g| < 0.4$ biases are limited to $|m| \lesssim 5\%$, still without recalibration compared to the work from Schrabback et al. (2010). Given that most of the weak lensing mass constraints for RCS2 J2327 originate from scales with $|g| < 0.2$, while the innermost radial bins that are included have $|g| < 0.4$ (see Sect. 5), we assume an intermediate 4% systematic uncertainty on the shear calibration for our systematic error budget. Based on the analysis from Hernández-Martín et al. (in prep.) we conclude that this shear calibration uncertainty results from a combination of limitations in the noise bias correction and a slight non-linear response of our KSB+ implementation for stronger shears, both of which can be fixed with a recalibration for potential future studies requiring a tighter systematic error control.

4.2. Photometry

For the HAWK-I K_s data all photometric measurements were conducted on the stack derived from all available exposures (see Sect. 3.1). We homogenised the PSF between the VLT and LBT stacks using spatially varying kernels constructed using `PSFEx` (Bertin 2011) and measured colours between these PSF-homogenised images employing 2.″0 diameter circular apertures. We used 2MASS (Skrutskie et al. 2006) K_s magnitudes for the absolute photometric calibration of the HAWK-I data. For the g and z bands we initially estimated zero points with respect to K_s using stellar locus regression. We then applied residual zero-point offsets to optimise the overlap of the galaxy colour distributions in $g - z$ vs. $z - K_s$ colour space between our catalogue and the UltraVISTA-detected reference catalogue used to estimate the redshift distribution (see Sect. 4.3)[3]. Photometric errors were estimated from the flux fluctuations when placing apertures at random locations that do not contain detected objects. For the 2.″0 diameter apertures we computed median 5σ limiting magnitudes[4] of (26.6, 25.9, 25.0) in the (g, z, K_s) bands. For the subsequent analysis we excluded regions near the edges of the HAWK-I mosaic and the LBT chip gaps as they have a significantly reduced depth in some of the bands. We also limited the subsequent analysis to galaxies with `SExtractor` "auto" magnitudes in the range $21 < K_s^{\rm tot} < 24.2$, given that brighter magnitude bins contain very few background galaxies, while the sample becomes highly incomplete at fainter magnitudes given the shape cuts (compare to the top panel of Fig. 2).

4.3. Reference samples to estimate the source redshift distribution

For unbiased mass measurements we have to accurately estimate the weighted-average geometric lensing efficiency $\langle\beta\rangle$ (see Eq. (4)) of the selected source sample. Here, a photometric selection of the lensed background galaxies helps to increase the measurement sensitivity, while reducing systematic uncertainties arising from cluster member contamination. Similar to the strategy from S18 we employed a colour selection (see Sect. 4.4) that is designed to yield negligible residual contamination by cluster members and applied a consistent selection to well-calibrated reference data from deep fields to estimate the redshift distribution and $\langle\beta\rangle$ (see Sect. 4.5).

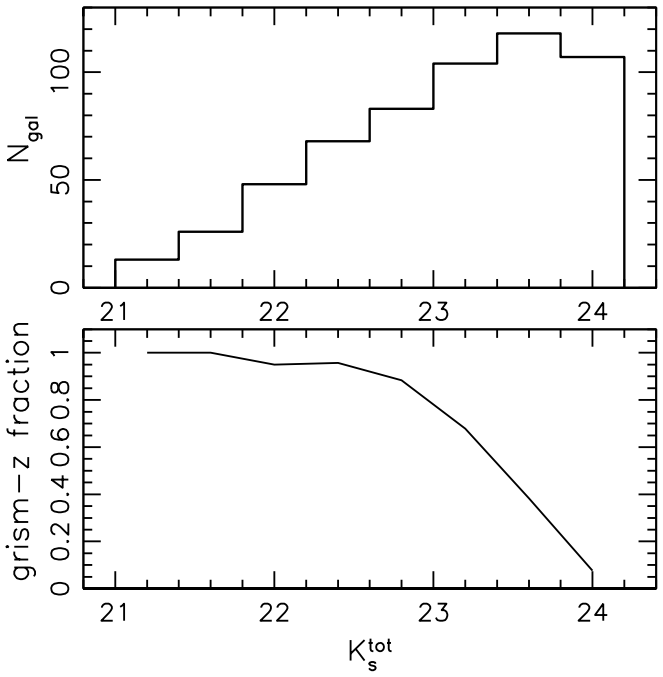

Fig. 2. *Top:* histogram of the number of colour-selected galaxies in our HAWK-I weak lensing shape catalogue (covering a non-masked area of 52.4 arcmin^2) as a function of the total K_s magnitude. *Bottom:* fraction of colour-selected galaxies within the CANDELS/COSMOS 3D-HST grism area with a robust HST grism redshift or spectroscopic redshift as a function of the total K_s magnitude from UltraVISTA.

4.3.1. UltraVISTA reference catalogue

The UltraVISTA Survey (McCracken et al. 2012) has obtained very deep NIR imaging in the COSMOS field (Scoville et al. 2007). By design the greatest depth is achieved in the "ultra-deep" stripes (McCracken et al. 2012), reaching a 5σ limiting K_s magnitude in 2.″0 apertures of 25.2 in the latest DR3 release, which exceeds even the depth of our HAWK-I imaging by 0.2 mag. COSMOS/UltraVISTA allows us to investigate galaxy colour and redshift distributions for our weak lensing analysis; the area of this survey (∼0.75 deg^2), which is 50 times larger than the HAWK-I field of view, greatly reduces uncertainties from sampling variance (see Sect. 4.5). In particular, we employed an updated version of the K_s-selected photometric redshift catalogue from Muzzin et al. (2013), which makes use of the deeper UltraVISTA DR3 data (see Muzzin et al., in prep. for details). In addition to the PSF-matched aperture magnitudes in g, z, and K_s used for colour measurements, we made use of the `SExtractor` "auto" magnitudes $K_s^{\rm tot}$. For our study we limited the analysis to objects that are photometrically classified as galaxies, located in non-masked areas of the "ultra-deep" stripes, and that are not flagged as blends by `SExtractor`.

While our HAWK-I+LBC catalogue and the UltraVISTA-detected catalogue have the same median depth in g (within 0.05 mag), the UltraVISTA-detected catalogue is deeper by 0.2 mag in K_s and shallower by 0.5 mag in z. We expect that the small difference in K_s depth would be negligible for our analysis, but to further improve the matching in the source selection between the two catalogues, we added Gaussian noise to

[3] This is necessary for two reasons. First, differences in the effective filter curves between our HAWK-I+LBC data and the VISTA+Subaru data used for the UltraVISTA reference catalogue lead to small differences in the colour calibration for stars and galaxies. Second, small zero-point offsets have already been applied to the UltraVISTA reference catalogue to improve the photo-z performance (see Muzzin et al. 2013).

[4] We quote limiting magnitudes without aperture correction.

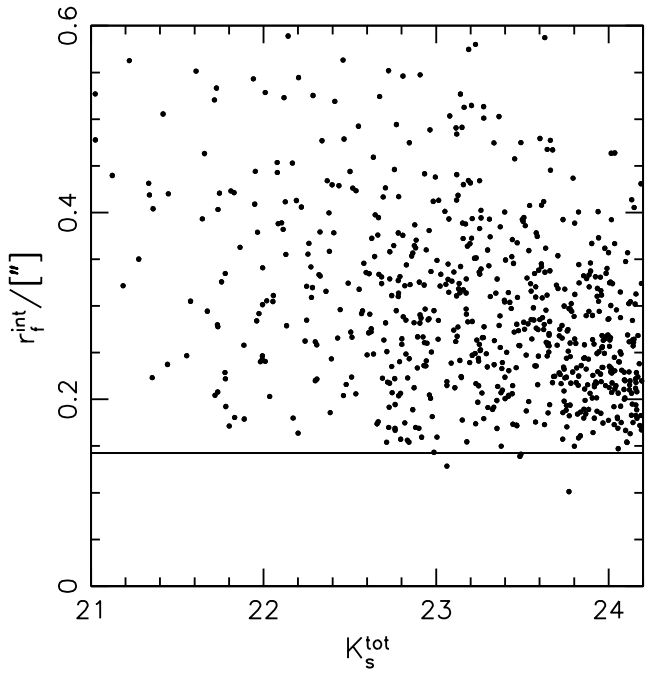

Fig. 3. Intrinsic flux radius r_f^{int} as measured in HST/WFC3 H-band data for galaxies in the CANDELS/COSMOS 3D-HST grism area passing our colour selection as a function of K_s^{tot}. The horizontal line corresponds to the mean size cut in our HAWK-I weak lensing analysis.

the UltraVISTA K_s^{tot} magnitudes to have identical limiting magnitudes; we also explicitly account for the incompleteness of the lensing catalogue when computing $\langle\beta\rangle$ in Sect. 4.5.1. The impact of differences in the noise in the colour measurement is investigated in Sect. 4.5.3.

4.3.2. 3D-HST reference catalogue

As a second reference data set to infer the source redshift distribution we employed redshifts computed by the 3D-HST team for galaxies in the CANDELS (Grogin et al. 2011; Koekemoer et al. 2011) area within the COSMOS field. This includes HST/NIR-selected photometric redshifts based on a total of 44 different photometric data sets (Skelton et al. 2014) and "grism"-redshift estimates from WFC3/IR slitless spectroscopy (Momcheva et al. 2016), where we also include ground-based spectroscopic redshifts compiled in the 3D-HST catalogue. Given the deeper NIR photometry and the deep grism spectra, these redshifts are expected to be highly robust, allowing us to conduct important cross-checks for our analysis. After applying our magnitude and colour selection (explained in Sect. 4.4) we find that 99.4% of the galaxies in the UltraVISTA-detected catalogue within the area covered by the grism spectra have a match in the 3D-HST catalogue[5]. The bottom panel of Fig. 2 shows the fraction of these galaxies that have a spectroscopic redshift or a 3D-HST grism redshift classified as robust by Momcheva et al. (2016) as a function of K_s^{tot} from UltraVISTA. Most galaxies at $K_s^{tot} \lesssim 23$ have a grism/spec-z, but this fraction drops at fainter magnitudes because of a combination of the magnitude limit $[JH] < 24$ employed by Momcheva et al. (2016), who used a $J + H$ band stack for detection and selection, and increased incompleteness at fainter magnitudes due to contamination by other objects. Nevertheless, when accounting for the K_s^{tot} distribution of our HAWK-I data and taking lensing weights into account (see Sect. 4.8), we find that effectively $\simeq$71% of the relevant galaxies in the 3D-HST grism area have a robust grism/spec-z. For comparison, the corresponding fraction amounts to only 21% for optically selected weak lensing source galaxies as employed in S18, with shape measurements from ACS $F606W$ data of single-orbit depth and a full-depth $V_{606} - I_{814}$ colour selection. Given the much higher fraction of grism/spec-z in the current study, we have to rely less on the accuracy of photometric redshift reference samples, leading to lower systematic uncertainties in the lensing analysis from the calibration of the redshift distribution (see Sect. 4.5.3). For our analysis we define a "best" redshift z_{best} from the 3D-HST catalogue, which is the spectroscopic or grism redshift of a galaxy when available and its photometric redshift otherwise.

Skelton et al. (2014) also provided HST/WFC3-measured H-band size estimates of CANDELS galaxies, allowing us to check if the galaxy size selection applied in our HAWK-I analysis has a relevant impact on the estimation of the redshift distribution. Figure 3 shows the distribution of the intrinsic flux radius $r_f^{int} = \sqrt{r_f^2 - r_{f,PSF}^2}$, defined via the flux radius parameter of the galaxies and stars from `SExtractor`, for the colour-selected CANDELS galaxies as a function of K_s^{tot}. This shows that ~99.4% of the galaxies are sufficiently resolved for shape measurements at the resolution of our HAWK-I data (limit illustrated as horizontal line in Fig. 3). As a result, the application of the size selection has a negligible impact on the estimated average geometric lensing efficiency. However, we stress that many of the galaxies are only slightly more extended than required for the shape analysis (see Fig. 3). We therefore recommend that similar programmes in the future do not relax the seeing requirements, compared to our study, in order to not suffer from a reduced weak lensing source density.

4.3.3. Redshift comparison

We compared the 3D-HST z_{best} redshifts to the peak photometric redshifts z_p from the UltraVISTA-detected catalogue in Fig. 4. While most galaxies closely follow the one-to-one relation[6], there are some noticeable systematic features visible. Here we focus on those galaxies that pass our colour selection shown in black. In particular, galaxies close to the one-to-one relation with $1.4 \lesssim z_{best} \lesssim 2.2$ appear to have a peak photometric redshift z_p in the UltraVISTA-detected catalogue that is slightly biased high on average. For galaxies with $2.2 \lesssim z_{best} \lesssim 3.4$ this bias disappears for the galaxies close to the one-to-one relation, but there is a noticeable fraction of outliers with a z_p biased low, in some cases catastrophically with $z_p \lesssim 0.4$. Given that these biases are in opposite directions, their impact partially cancels when computing the average geometric lensing efficiency (see Sect. (4.5).

Indications for similar outliers have already been noted by Schrabback et al. (2010) and S18. In particular, S18 compare 3D-HST photo-zs to extremely deep photometric and grism redshifts

[5] The non-matching galaxies can be explained through differences in the deblending and have no relevant impact on our analysis.

[6] When defining catastrophic redshift outliers as $\Delta z = |z_{best} - z_p| > 1$, 5.5% of the colour-selected galaxies shown in Fig. 4 are catastrophic redshift outliers. Excluding these catastrophic outliers, the redshift scatter of the remaining galaxies can be quantified via the root mean square $\mathrm{rms}(\Delta z/[1 + z_{best}]) = 0.07$.

available in the HUDF. While S18 conclude that the 3D-HST photo-zs are biased low in this case, this is not in contradiction with our results given that the S18 analysis is based on blue optically selected samples, which are on average significantly fainter in the NIR compared to the galaxies studied here. We interpret the various results such that a noticeable fraction of catastrophic redshift outliers, in the form of high-z galaxies incorrectly assigned a low photo-z, can be present even if NIR photometry is available, unless that has a high signal-to-noise ratio. We expect that accounting for this effect will also be relevant when calibrating redshift distributions for wide-area weak lensing surveys, for example employing the approach from Masters et al. (2017). As the catastrophic outliers lead to a bimodality of the colour-redshift relation, highly complete spectroscopic redshift measurements will be needed in the relevant parts of colour-colour space to adequately map out this bimodality.

4.4. Colour selection

The left panel of Fig. 5 shows the distribution of resolved galaxies with $21 < K_s^{\rm tot} < 24.2$ within the CANDELS/COSMOS 3D-HST grism area in $g-z$ vs. $z-K_s$ colour space, with different symbols indicating different ranges in $z_{\rm best}$. The solid lines indicate our colour selection scheme, where we select background galaxies that have

$$z - K_s > \min[g - z, 2.5]. \quad (14)$$

This selection is similar to the BzK_s selection introduced by Daddi et al. (2004), but is slightly more conservative for the exclusion of galaxies around the cluster redshift. It is highly effective in selecting most of the background galaxies at $z_{\rm best} > 1.4$, while efficiently removing galaxies at $z_{\rm best} < 1.1$ (see Fig. 6). In particular, 98.1% of the colour-selected galaxies are in the background at $z_{\rm best} > 1.1$. At the same time, 98.9% of the galaxies in the parent catalogue at relevant cluster redshifts $0.6 < z_{\rm best} < 1.1$ are removed by this colour selection, providing an efficient suppression of cluster member contamination.

The right panel of Fig. 5 shows the distribution of galaxies in our HAWK-I+LBC shear catalogue in $g-z$ vs. $z-K_s$ colour space prior to the colour selection. In addition to the galaxy populations visible in the UltraVISTA-detected catalogue, this prominently displays the population of cluster red-sequence galaxies around $g-z \simeq 3$ and $z-K_s \simeq 1$.

4.5. Average geometric lensing efficiency

4.5.1. Best estimate

For the mass measurements we need to estimate the weighted-average geometric lensing efficiency (see Eq. (4)) of our source sample. We started with the colour- and size-selected galaxies in the 3D-HST grism area and computed $\langle\beta\rangle_i$ from the 3D-HST $z_{\rm best}$ redshifts in magnitude bins of width 0.4 mag within $21 < K_s^{\rm tot} < 24.2$, taking the $K_s^{\rm tot}$-dependent shape weights into account (see Sect. 4.8). We then computed a joint estimate $\langle\beta\rangle_{\rm 3D-HST}^{\rm grism-area} = \left(\sum_i \langle\beta\rangle_i \sum_{j(i)} w_j\right) / \left(\sum_i \sum_{j(i)} w_j\right) = 0.501$ according to the shape weights w_j of the galaxies in magnitude bin i in our HAWK-I catalogue. This procedure accounts for the greater incompleteness of the HAWK-I catalogue given the lensing S/N cut.

We quantified and minimised the impact of sampling variance using the UltraVISTA-detected catalogue. For this we employed the same colour selection and weighting scheme as for the 3D-HST catalogue, but this time we used the peak photometric redshift z_p and dropped the size selection due to the lack of HST NIR-measured sizes in COSMOS outside the CANDELS footprint. We then computed estimates both for the full UltraVISTA ultra-deep area ($\langle\beta\rangle_{\rm UltraVISTA}^{\rm full} = 0.470$) and the 3D-HST grism area ($\langle\beta\rangle_{\rm UltraVISTA}^{\rm grism-area} = 0.490$). The latter covers the same area that was used for the analysis employing the 3D-HST $z_{\rm best}$ redshifts. Accordingly, the ratio $r_{\rm sys} = \langle\beta\rangle_{\rm UltraVISTA}^{\rm grism-area} / \langle\beta\rangle_{\rm 3D-HST}^{\rm grism-area} = 0.978$ provides us with a correction factor $r_{\rm sys}^{-1}$ to account for the impact of the systematic redshift errors in the UltraVISTA-detected catalogue discussed in Sect. 4.3.3. This can be combined with the estimate from the full UltraVISTA ultra-deep area, which suffers less from sampling variance, to obtain our best estimate of the cosmic mean geometric lensing efficiency given our selection criteria of $\langle\beta\rangle_{\rm cor} = \langle\beta\rangle_{\rm UltraVISTA}^{\rm full} / r_{\rm sys} = 0.481$.

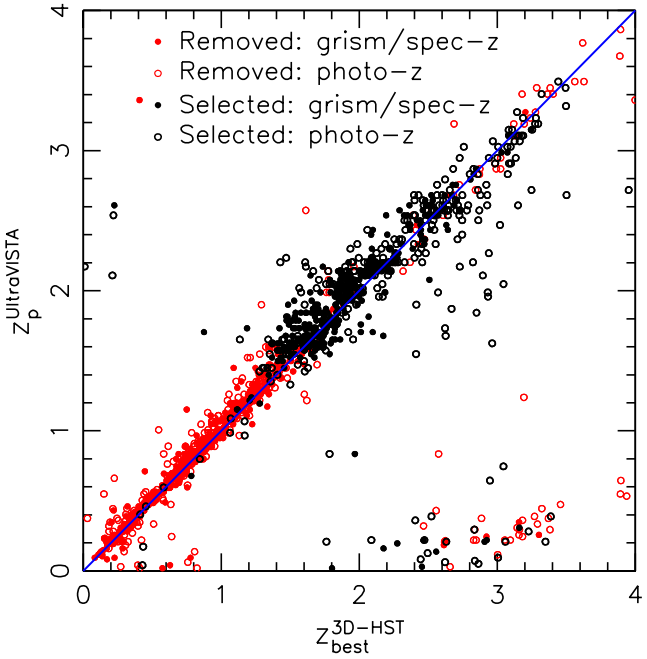

Fig. 4. Comparison of the best redshift estimate $z_{\rm best}$ from 3D-HST and the peak photometric redshift z_p in the UltraVISTA-detected catalogue for galaxies located in the area covered by the grism observations with $21 < K_s^{\rm tot} < 24.2$. Galaxies with a spectroscopic or grism redshift in the 3D-HST catalogue are indicated as filled circles, while the galaxies having a photometric redshift in the 3D-HST catalogue only are shown as open circles. Black symbols correspond to galaxies passing our colour selection, while red symbols show galaxies removed by the colour selection. The blue line shows the one-to-one relation.

4.5.2. Line-of-sight variations and $\langle\beta^2\rangle$

The redshift distribution within the sky patch covered by our HAWK-I observation likely deviates from the cosmic mean distribution because of sampling variance. To obtain an estimate for this effect we placed 12 tiles of the same area widely distributed over the area of the UltraVISTA ultra-deep stripes. From the variation between the $\langle\beta\rangle$ estimates computed from these tiles, we estimated a relative uncertainty of $\Delta\langle\beta\rangle / \langle\beta\rangle = 2.2\%$

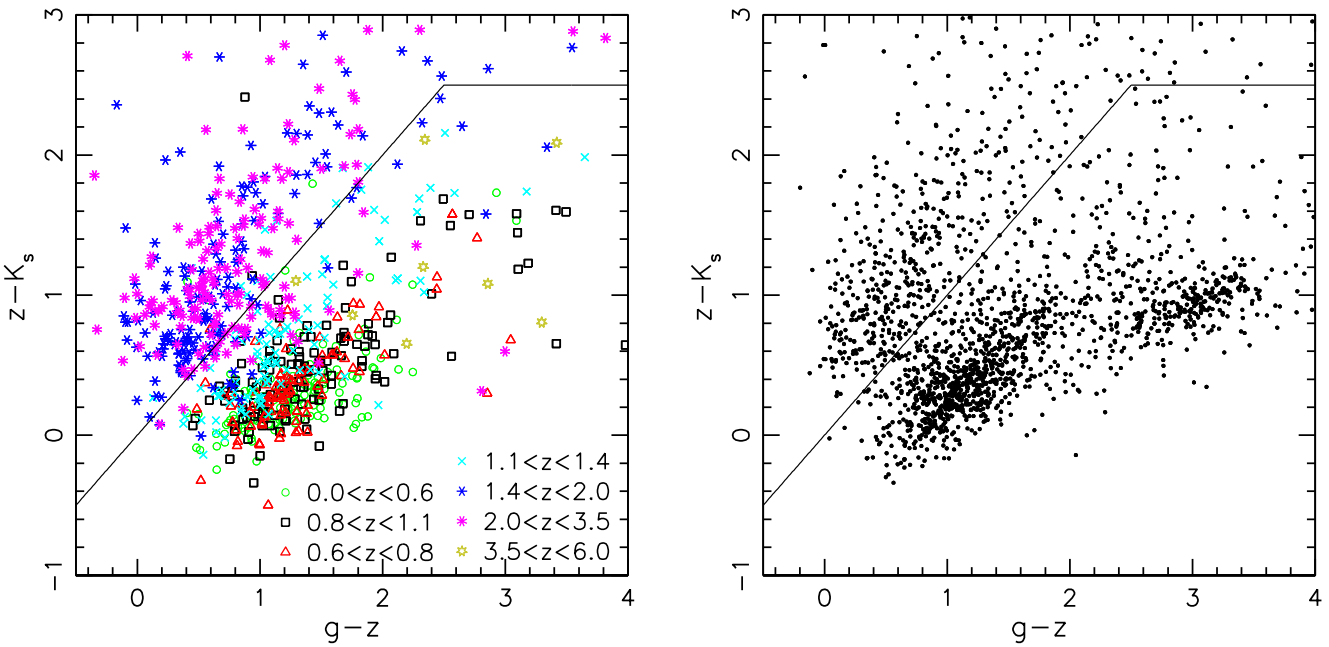

Fig. 5. Distribution of galaxies with $21 < K_s^{tot} < 24.2$ passing our size selection in $g - z$ vs $z - K_s$ colour space. The black line indicates the colour selection $z - K_s > \min[g - z, 2.5]$ employed in our analysis. The *left panel* shows a random 50% fraction of the galaxies in the CANDELS/COSMOS 3D-HST grism area, with colours and symbols indicating various ranges in the best redshift estimate from 3D-HST. The *right panel* shows the galaxies passing the shape selection in our catalogue for RCS2 J2327. The excess of galaxies around $g - z \simeq 3$ and $z - K_s \simeq 1$ corresponds to the cluster red sequence, which is efficiently removed from our background sample, along with bluer cluster members located near $g - z \simeq 1.2$ and $z - K_s \simeq 0.3$.

for our analysis (for a single cluster[7]) arising from line-of-sight variations in the redshift distribution.

We accounted for the impact of the finite width of the source redshift distribution in the lensing analysis following Hoekstra et al. (2000), for which we also require an estimate of the weighted $\langle\beta^2\rangle = 0.237$, which we computed based on the 3D-HST z_{best} redshifts (given the z_p outliers), but rescaled with the factor $\left(\langle\beta\rangle^{full}_{UltraVISTA}/\langle\beta\rangle^{grism\text{-}area}_{UltraVISTA}\right)^2$ to account for the impact of sampling variance.

4.5.3. Systematic uncertainties

The 3D-HST-derived $\langle\beta\rangle$ estimates are expected to be highly robust, as they are mostly based on accurate grism or spectroscopic redshifts (to ∼71% when accounting for our weighting scheme, see Sect. 4.3.2). However, we cannot fully exclude the possibility that the ∼29% contribution from 3D-HST photo-z may introduce systematic uncertainties because of photo-z biases. To obtain an approximate estimate for this uncertainty, we recomputed $\langle\beta\rangle^{grism\text{-}area}_{3D\text{-}HST}$ using the 3D-HST photometric redshifts for all galaxies, hence using 100% photo-z information instead of 29%. This leads to a very small relative increase in $\langle\beta\rangle$ by 0.4%. The expected systematic uncertainty associated with the use of ∼29% photo-z uncertainty, on the one hand, would be lower than this number given the smaller fraction of employed photo-zs, but, on the other hand, would be larger given that these galaxies are typically fainter. Considering both aspects, we expect that 0.4% likely corresponds to a reasonably realistic estimate of the resulting residual uncertainty.

Additional systematic biases in $\langle\beta\rangle$ may arise from mismatches in the photometric calibration or matching of noise

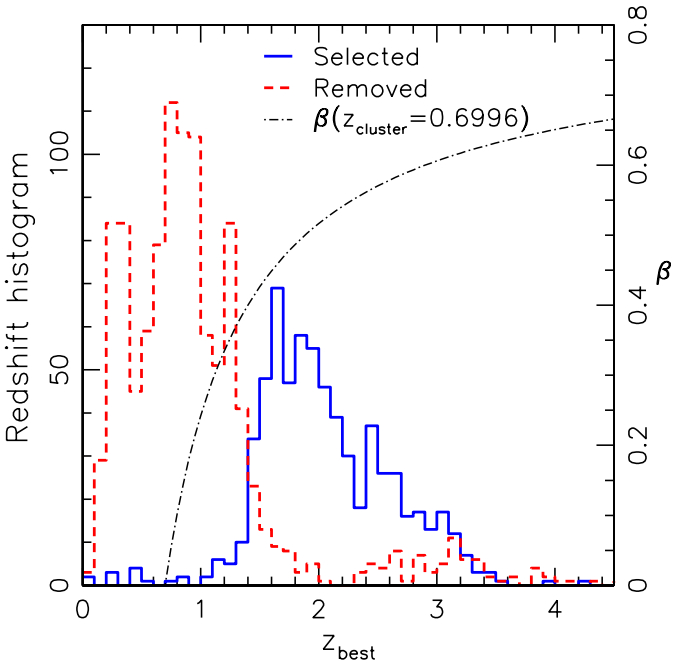

Fig. 6. Histogram of the best 3D-HST redshift estimate for sufficiently resolved galaxies with $21 < K_s^{tot} < 24.2$ within the CANDELS/COSMOS 3D-HST grism area, split between galaxies selected and removed by our gzK_s selection. The dash-dotted curve shows the geometric lensing efficiency β as a function of source redshift.

[7] A potential future scaling relation analysis that incorporates observations from a large number of clusters would have a systematic uncertainty arising from line-of-sight variations in the redshift distribution that is approximately reduced by a factor $1/\sqrt{12} \simeq 0.29$, assuming large-scale structure at high redshifts is sufficiently uncorrelated between the 12 tiles.

properties. To quantify the impact of the former, we tested the sensitivity to systematic errors in the colour measurements. We find that a systematic error in $g - z$ or $z - K_s$ colour of 0.1 mag, which provides a conservative estimate for the uncertainty in the colour calibration, leads to a relative bias in $\langle\beta\rangle$ of only 0.5%.

The matching of noise properties is complicated by the fact that our HAWK-I+LBC observations are slightly shallower in the K_s band than the reference catalogue, but deeper in the z band (see Sect. 4.3.1). Hence, we cannot simply add noise to the colours in the reference catalogue as performed for K_s^{tot}. However, since the colour selection already achieves an excellent selection of background galaxies at the depth of the UltraVISTA-detected catalogue (Fig. 6), we expect that this is also the case for colour estimates with slightly higher signal-to-noise ratio. In order to roughly estimate the sensitivity of our analysis to noise in the colour measurements, we randomly added Gaussian scatter corresponding to a depth difference of 0.3 mag separately to the g, z, and K_s fluxes of the UltraVISTA-detected catalogue, finding that this leads to relative changes in $\langle\beta\rangle$ of +0.0%, −0.2%, and −0.1%, respectively. Biases at these levels are completely negligible compared to the statistical uncertainties of our study. Added in quadrature, the systematic errors for the $\langle\beta\rangle$ estimate identified in this subsection amount to 0.7%.

4.6. Choice of centre

For our weak lensing shear profile analysis we have to adopt a centre. This should match the position of the centre of the projected mass distribution as best as possible to minimise miscentring uncertainties (see e.g. Schrabback et al. 2018). For RCS2 J2327 the centre of the inner projected mass distribution is very well constrained by strong gravitational lensing to a location $1\farcs17^{+0\farcs47}_{-0\farcs24}$ east and $7\farcs42^{+1\farcs42}_{-0\farcs63}$ north from the brightest cluster galaxy (BCG), in the direction towards the second brightest cluster galaxy (Sharon et al. 2015). This very small positional uncertainty is completely negligible for weak lensing studies (e.g. compare to von der Linden et al. 2014). We therefore fix the centre position for our analysis to the best-fitting centre position of the strong lensing analysis from Sharon et al. (2015) at $(\alpha, \delta) = (351.865351, -2.074863)$ deg.

4.7. Number density profile

As shown in Sect. 4.4 our colour selection is expected to lead to a negligible residual contamination by cluster galaxies in the source sample. As a consistency check for this, we investigated the radial source number density profile. Because of the central concentration of cluster galaxies, a substantial residual contamination would be detectable as an increase in the source density towards the centre. For our catalogue we do not detect such a central increase. As shown in Fig. 7, the source density profile is approximately flat for radii $r \gtrsim 0.6$ Mpc with a global mean density of 9.8 arcmin^{-2}.

Further into the cluster core the observed source density drops (see Fig. 7). We suspect that this may be due to a combination of two effects. First, we cannot detect faint background galaxies behind or close to a bright foreground cluster galaxy. In order to account for this effect at least approximately, we used a bright objects mask for the sky area calculation (already taken into account in Fig. 7, causing a ∼7% correction in the inner bins together with the manual masks). We created this by running `SExtractor` with a high object detection threshold of 200 pixels exceeding the background by 1.5σ and then used the "objects"

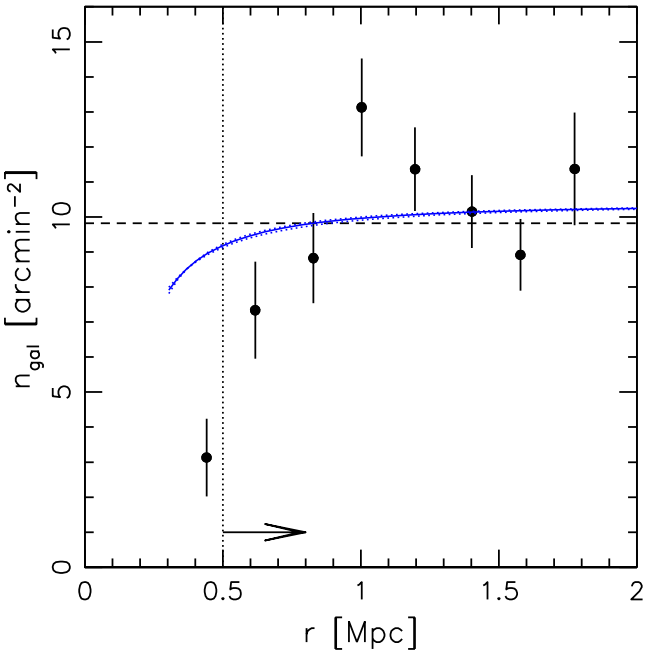

Fig. 7. Source density in our colour- and magnitude-selected weak lensing source catalogue for RCS2 J2327 as a function of projected distance from the cluster centre, taking field boundaries, manual masks, and a bright objects mask into account. Error bars are underestimated, as they assume Poisson galaxy counts ignoring spatial clustering. The dashed black line indicates the average density over the whole field of view, while the blue curves indicate the approximately expected profile due to lensing magnification assuming the best-fitting NFW model for $c_{200c} = 5.1$ (solid) or $c_{200c} \in [4.1, 6.1]$ (dotted, close to the solid curve). The vertical black dotted line and the arrow indicate the lower radial limit in the weak lensing shear profile fit.

check image as a mask. However, as this mask neither accounts for fainter cluster members nor the outer wings of galaxy light profiles or the impact of intra-cluster light, it likely still leads to an underestimation of the inner source density.

Second, we suspect that lensing magnification may also lead to a net depletion in the density of faint sources. This has the largest impact in the stronger magnification regime of cluster cores (see e.g. Fort et al. 1997). Assuming source counts described by a power law and sources at a single redshift, magnification leads to a net depletion in the source counts if the slope of the logarithmic cumulative number counts is shallow,

$$s = \frac{\mathrm{d}\log_{10} N(<m)}{\mathrm{d}m} < 0.4 \tag{15}$$

(e.g. Broadhurst et al. 1995; Mayen & Soucail 2000). We computed this slope for the colour-selected UltraVISTA-detected catalogue around $m = K_s^{tot} \simeq 24$ mag, yielding $s = 0.32 \pm 0.02$ assuming negligible incompleteness, which is indeed consistent with an expected depletion. Making the same simplifying assumptions we plot the expected source density profile resulting from magnification as solid blue curve in Fig. 7, employing the best-fit NFW density profile from our reduced shear profile fit (see Sect. 5.2). This indicates that magnification alone likely cannot explain the very low source density at $r \simeq 0.45$ Mpc, but that additional effects, such as the limitations in the bright objects mask may dominate. In addition, it may just be that the line of sight behind the core of RCS2 J2327 is noticeably underdense. In this respect, the error bars shown in Fig. 7 assume Poisson source counts but ignore spatial clustering, which underestimates

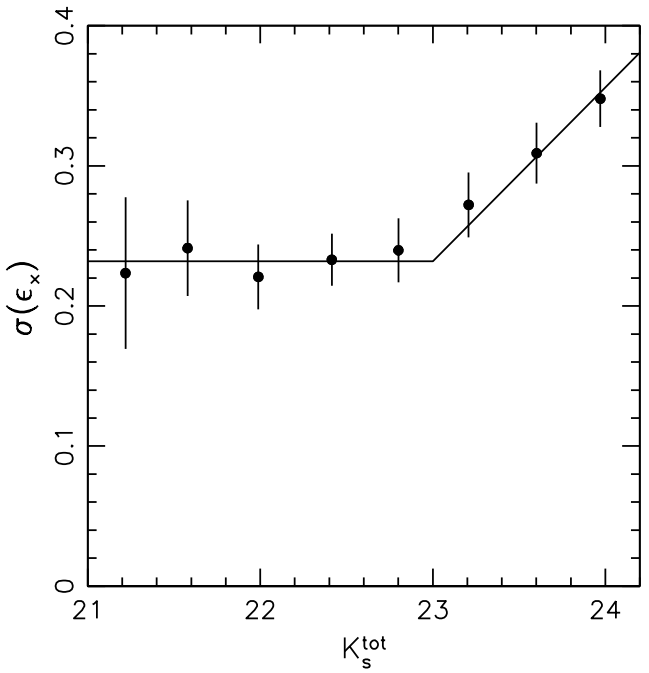

Fig. 8. Dispersion of the cross-ellipticity component with respect to the cluster centre computed in bins of K_s^{tot} including all lensing and colour-selected galaxies with a projected separation $r > 700$ kpc from the cluster centre. The solid line shows our approximate fit that is used to define shape weights.

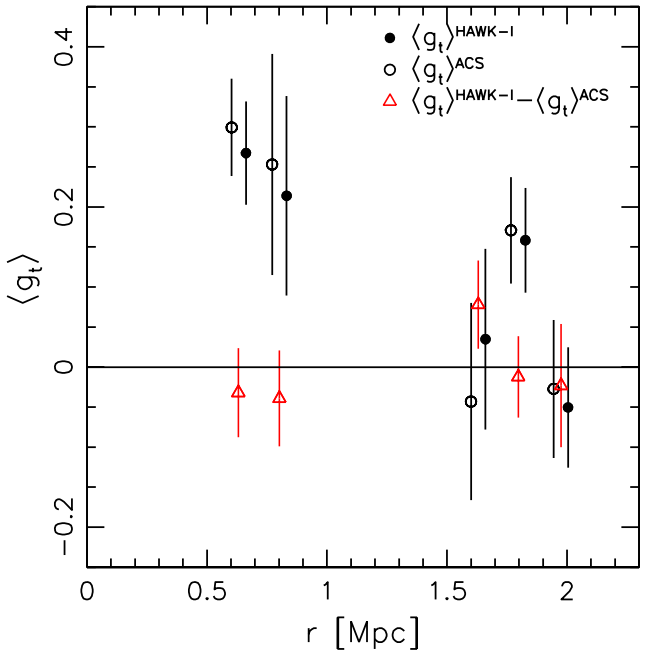

Fig. 9. Profile of the estimated tangential reduced shear for RCS2 J2327, based on the matched HAWK-I and ACS ellipticity catalogue, employing the HAWK-I+LBC colour selection and uniform weights. We show all radial bins containing at least five galaxies. The solid (open) points are based on the HAWK-I (ACS) ellipticity measurements, shown with an offset of +30 kpc (−30 kpc) for clarity. The red open triangles indicate the difference between the two estimates with error bars determined by bootstrapping the sample. Matched data are only available in the central ACS pointing and near the corners of the HAWK-I field of view. The resulting smaller area and lower source density leads to more noisy data compared to the analysis of the full HAWK-I+LBC-based catalogue (compare Fig. 12) and introduces the gap at intermediate radii.

the true uncertainty and therefore overestimates the significance of the data point, as especially relevant at small radii.

4.8. Shape noise and shape weights

At fixed redshift, fainter sources tend to result in more noisy shear estimates than bright sources, for two reasons. First, the higher measurement noise leads to more noisy ellipticity measurements. Second, as shown by S18, in optically selected samples the dispersion of the intrinsic source ellipticity increases at faint magnitudes, further increasing the noise in the shear estimate. As we show below and discuss in Sect. 6, the K_s imaging yields shape estimates for high-z galaxies with a lower measured ellipticity dispersion, indicating a lower intrinsic ellipticity dispersion than for optical high-z samples.

To account for the more noisy shear estimates at faint magnitudes, S18 employed an empirical weighting scheme according to the ellipticity dispersion measured in non-cluster fields as a function of magnitude. Given the presence of a massive cluster, which significantly shears the background galaxy images, we cannot directly apply the same approach here. However, as the cluster lensing signature primarily affects the tangential ellipticity component ϵ_t with respect to the cluster centre, but not the cross-component $\epsilon_\times$, we can use the measured dispersion of the cross-ellipticity component $\sigma_{\epsilon,\times} = \sigma(\epsilon_\times)$ as a function of K_s^{tot} (shown in Fig. 8) to define the weighting scheme. We find that $\sigma_{\epsilon,\times}(K_s^{tot})$ is approximately flat for $K_s^{tot} < 23$ with

$$\sigma_{\epsilon,0} \equiv \sigma_{\epsilon,\times}\left(21 < K_s^{tot} < 23\right) = 0.232 \pm 0.011 \quad (16)$$

and increases approximately linearly as

$$\sigma_{\epsilon,\times}\left(K_s^{tot}\right) = \sigma_{\epsilon,0} + (0.124 \pm 0.009)\left(K_s^{tot} - 23\right) \quad \text{for } K_s^{tot} > 23. \quad (17)$$

We expect that this increase is mostly caused by measurement noise, but we cannot exclude a possible contribution from an increase in the intrinsic ellipticity dispersion at faint magnitudes. We use $w\,(K_s^{tot}) = \sigma_{\epsilon,\times}^{-2}\,(K_s^{tot})$ as shape weight.

The K_s-measured ellipticity dispersion is significantly lower than what has been found by S18 for galaxies at similar redshifts with a largely identical shape measurement pipeline analysing optical HST/ACS images of approximately single-orbit depth. At a relatively bright magnitude $V_{606,auto} = 25$, where the contribution from measurement noise is small, S18 estimate $\sigma_\epsilon = 0.306$ for a $V_{606} - I_{814} < 0.3$ colour-selected sample. This is significantly larger than the K_s-measured σ_ϵ at bright magnitudes (Eq. (16)).

4.9. Comparison to HST/ACS weak lensing shear estimates

To cross-check our HAWK-I shear estimates we compared these to measurements from overlapping HST/ACS observations (see Sect. 3.3). For the ACS catalogue generation we employed the same basic KSB+ implementation as for the HAWK-I shape measurements (see Sect. 4.1), but additionally included the principal component PSF interpolation from Schrabback et al. (2010) (building on Jarvis & Jain 2004) and the PSF model calibration and shape weighting scheme from S18. For the central ACS pointing, the weak lensing catalogue generation has also been described in Hoag et al. (2015).

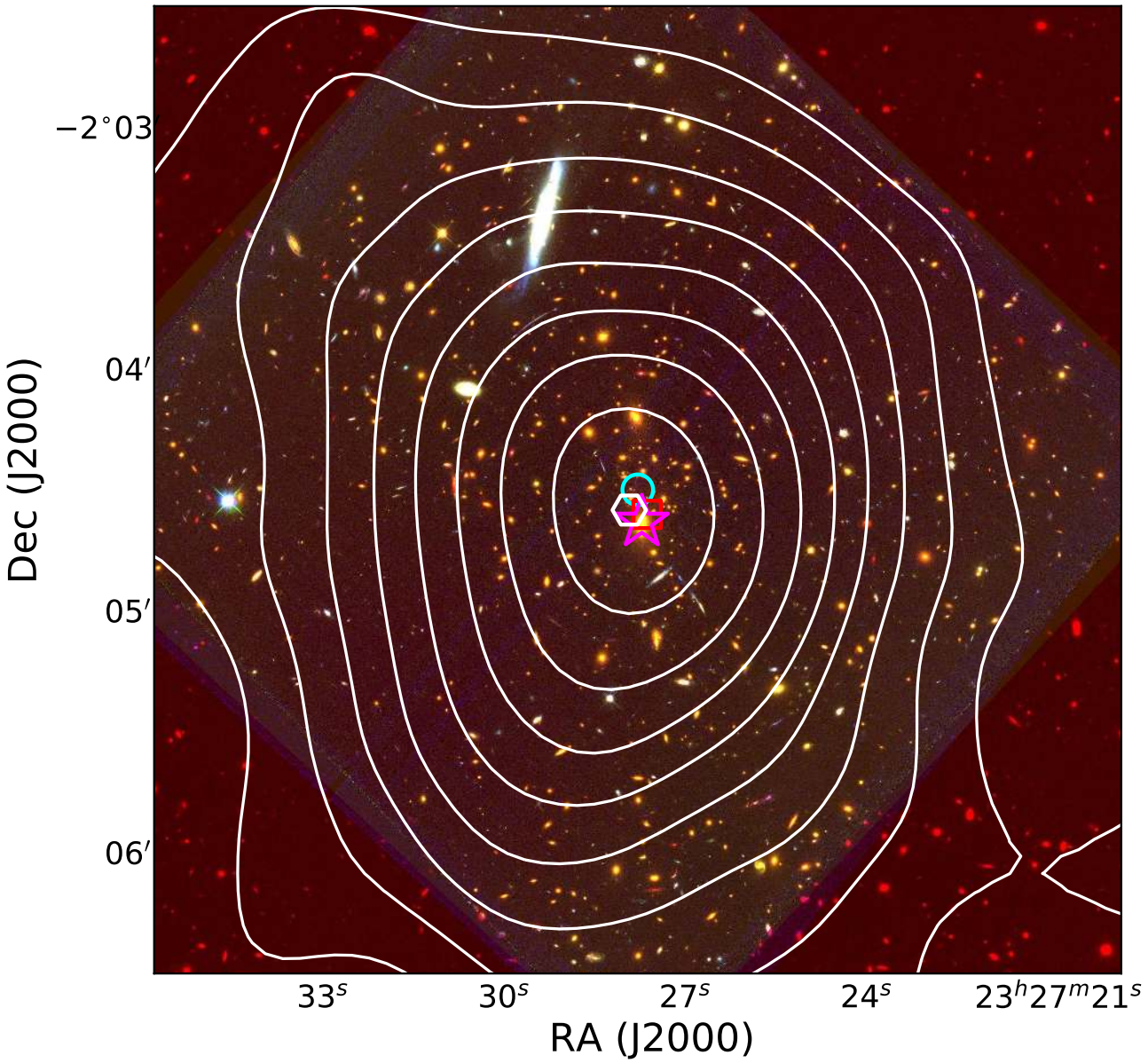

Fig. 10. RGB colour image of the central $4' \times 4'$ of RCS2 J2327 created from the VLT/HAWK-I K_s best-seeing stack and the HST/ACS $F814W$ and $F435W$ images. The contours indicate the weak lensing convergence reconstruction starting at $\kappa_0 = 0.04$ in steps of $\Delta\kappa = 0.04$ with the peak indicated by the white hexagon. The magenta star, red square, and cyan circle indicate the locations of the BCG, the peak in the X-ray emission, and the strong lensing centre from Sharon et al. (2015), respectively.

When comparing shape measurements obtained with different resolution and/or in different band passes, a direct comparison of ellipticity estimates is not an adequate metric, as the spatial distribution of the light emission may not be identical and different effective radial weight functions are used. This is underlined by the indications we find for a significantly lower intrinsic ellipticity dispersion for the analysis based on K_s imaging compared to ACS optical imaging (see Sect. 4.8). Nevertheless, what should be consistent is the estimated reduced tangential cluster shear profile when a matched catalogue with identical weights is used. This is shown in Fig. 9, where we employ the HAWK-I+LBC colour selection and uniform weights for the galaxies in the matched HAWK-I and ACS ellipticity catalogue. As the difference in the reduced shear estimates $\langle g_t \rangle^{\mathrm{HAWK-I}} - \langle g_t \rangle^{\mathrm{ACS}}$ is consistent with zero, we conclude that the HAWK-I and ACS measurements are fully consistent within the current statistical uncertainty.

5. Cluster weak lensing results

5.1. Mass reconstruction

We reconstructed the convergence (κ) distribution of RCS2 J2327 on a grid, using an improved version of the Kaiser & Squires (1993) formalism, which applies a Wiener filter as described in McInnes et al. (2009) and Simon et al. (2009), and as further detailed in S18. Given the mass-sheet degeneracy we cannot constrain the average convergence in the field of view. We fixed it to zero, which is adequate for large fields of view, but likely leads to an underestimation for our data.

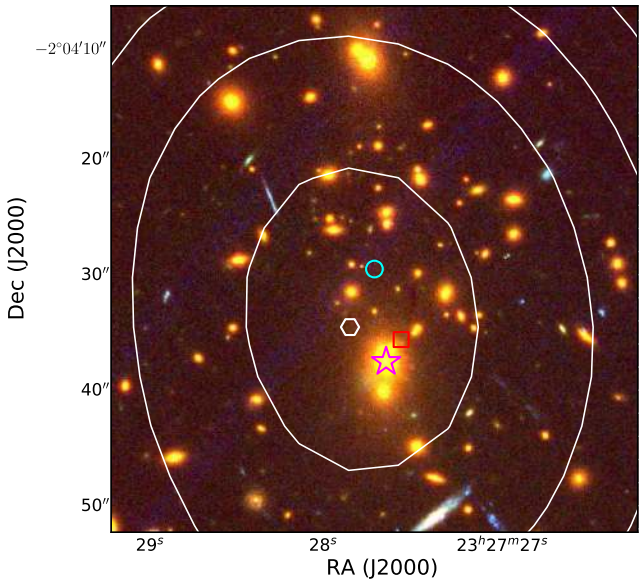

Fig. 11. As Fig. 10, but showing a cut-out of the central $45'' \times 45''$ with contours in steps of $\Delta\kappa = 0.02$, where the innermost contour corresponds to $\kappa = 0.34$.

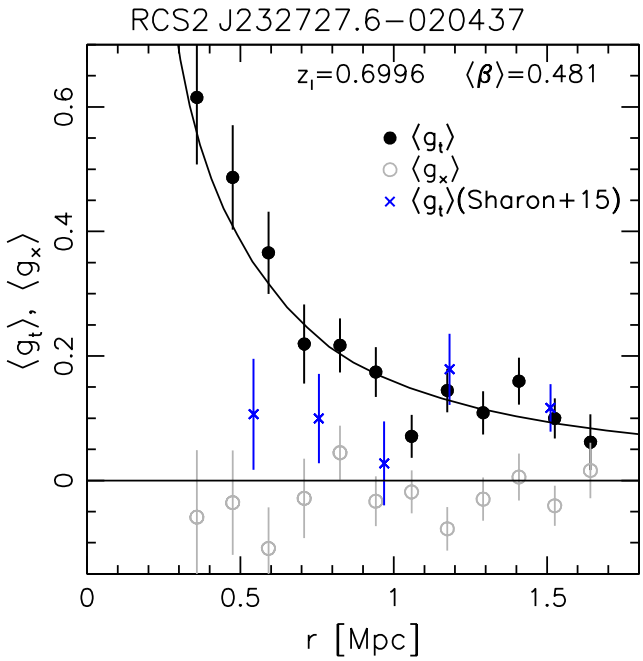

Fig. 12. Profile of the tangential reduced shear (filled circles) and the 45 degrees-rotated cross-component (open circles) for RCS2 *J*2327 as function of cluster-centric separation. The solid curve shows the best-fitting NFW model prediction for a fixed concentration $c_{200c} = 5.1$ when considering scales 500 kpc $< r <$ 1.6 Mpc. The blue crosses indicate tangential reduced shear estimates from Sharon et al. (2015) based on deep CFHT weak lensing measurements, scaled to the same $\langle\beta\rangle$ and excluding points at small radii that are not included in their fit. Sharon et al. (2015) also incorporate measurements at larger radii that are not shown here.

This uncertainty is however not a concern for our analysis as we use the mass reconstruction only for illustration and consistency checks regarding the location of the cluster centre. Given the high cluster mass we apply an iterative reduced-shear correction (e.g. Seitz & Schneider 1996) based on the κ distribution from the previous iteration. Figure 10 shows contours of the resulting reconstruction starting at $\kappa_0 = 0.04$ in steps of $\Delta\kappa = 0.04$, with a peak value $\kappa_{\rm max} = 0.347$.

To estimate the peak significance we apply the same reconstruction algorithm to noise catalogues generated by randomising the ellipticity phases. Dividing the reconstruction from the real data through the rms image of the noise reconstructions we estimate a 10.1σ peak significance. In Fig. 10 the contours are overlaid on an RGB colour image based on the HAWK-I $K_{\rm s}$ and the ACS $F814W$ and $F435W$ images, with indications of the BCG, as well as the strong lensing centre and the peak of the X-ray emission from Sharon et al. (2015). The peak of the weak lensing κ-reconstruction at $(\alpha, \delta)_{\rm peak} = (351.86594, -2.07626)$ deg is constrained to $(\Delta\alpha, \Delta\delta)_{\rm peak} = (3\farcs2, 5\farcs7)$ as estimated by bootstrapping the source catalogue, making it consistent with the locations of the BCG, X-ray centre, and strong lensing centre (see also Fig. 11) within $\sim 1\sigma$.

5.2. Reduced shear profile analysis and mass constraints

Weak lensing measurements can provide non-parametric estimates of projected cluster masses via the aperture mass statistic (e.g. Hoekstra et al. 2015) if the lensing signal is measured well beyond the cluster virial radius. As the HAWK-I field of view does not provide such a large radial coverage for RCS2 *J*2327, we instead have to rely on model fits of the cluster tangential reduced shear profile to constrain the cluster mass. This effectively breaks the mass-sheet degeneracy discussed in Sect. 5.1. In practise, such idealised mass sheets are related to correlated and uncorrelated large-scale structure projections. The net impact of such projections for weak lensing mass estimates is additional scatter, as computed and discussed below.

We show the tangential reduced shear profile of RCS2 *J*2327 as a function of separation from the strong lensing centre[8] (see Sect. 4.6) as estimated from our HAWK-I+LBT catalogue in Fig. 12. We fit these data using reduced shear profile predictions from Wright & Brainerd (2000) assuming a spherical NFW density profile (Navarro et al. 1997). We only consider radii in the range 500 kpc $< r <$ 1.6 Mpc. At smaller radii the measured tangential reduced shear exceeds the regime tested in the weak lensing image simulations (see Sect. 4.1). At larger scales the azimuthal coverage gets increasingly incomplete.

The weak lensing data alone cannot constrain the cluster concentration c_{200c} sufficiently well, which is why we revert to results from numerical simulations. Using a suit of simulations, Diemer & Kravtsov (2015) provided a well-calibrated prescription to compute the expected mean halo concentration as a function of mass, which would be adequate for a general cluster. However, the X-ray analysis from Sharon et al. (2015) indicated that RCS2 *J*2327 is a fairly relaxed cluster, which is why, on average, a higher concentration should be expected than for a general cluster. Neto et al. (2007) investigated the difference in structural parameters for relaxed vs. general simulated dark matter haloes at redshift $z = 0$. They find that haloes at the mass-scale of RCS2 *J*2327 have on average larger median concentrations compared to general haloes by a factor 1.16. Assuming that this factor also holds at higher redshifts, we conducted a two-step fit for RCS2 *J*2327: first, we fit the

[8] We do not centre on the peak of the weak lensing mass reconstruction from Sect. 5.1 as this is expected to yield mass constraints that are biased high (e.g. Dietrich et al. 2012). However, this would likely be a minor effect given our very high-significance detection.

data assuming the concentration–mass relation from Diemer & Kravtsov (2015), yielding a best-fit cluster mass that corresponds to a mean $c_{200c,D15} = 4.4$. Based on the results from Neto et al. (2007) we then repeated the fit assuming a larger concentration $c_{200c} = 1.16\, c_{200c,D15} = 5.1$ yielding

$$M_{200c}/(10^{15}\ M_\odot) = 2.06^{+0.28}_{-0.26}(\text{stat.}) \pm 0.12(\text{sys.}), \quad (18)$$

where the statistical error contains contributions added in quadrature from shape noise ($^{+0.21}_{-0.20} \times 10^{15}\ M_\odot$), large-scale structure projections ($\pm 0.12 \times 10^{15}\ M_\odot$) as estimated in S18, line-of-sight variations in the source redshift distribution ($\pm 0.07 \times 10^{15}\ M_\odot$; see Sect. 4.5), and the impact of the uncertainty in the concentration ($^{+0.12}_{-0.10} \times 10^{15}\ M_\odot$). We derive the latter uncertainty from the estimated scatter in the logarithm of the concentration $\sigma(\log_{10} c_{200c}) = 0.061$ for high-mass relaxed haloes as found by Neto et al. (2007). The systematic error in Eq. (18) is dominated by the shear calibration ($\pm 0.12 \times 10^{15}\ M_\odot$; see Sect. 4.1) with a minor contribution from the systematic uncertainty of the $\langle\beta\rangle$ estimate ($\pm 0.02 \times 10^{15}\ M_\odot$; see Sect. 4.5.3). Based on the M_{200c} limits and fixed concentration we also report mass constraints for an overdensity $\Delta = 500$ of

$$M_{500c}/(10^{15}\ M_\odot) = 1.50^{+0.19}_{-0.17}(\text{stat.}) \pm 0.09(\text{sys.}), \quad (19)$$

taking the same sources of uncertainty into account. The sensitivity to the uncertainty in the concentration is lower for M_{500c} (3% relative uncertainty) than for M_{200c} (5% relative uncertainty). While the weak lensing data cannot constrain the radii corresponding to the considered overdensities Δ separately, we list the best-fitting values $r_{200c} = 2.03$ Mpc and $r_{500c} = 1.34$ Mpc given the assumed concentration to simplify possible mass comparisons in future studies.

Our assumptions regarding the concentration–mass relation are also consistent with recent findings from the CLASH project (Postman et al. 2012). In particular, the constraints derived by Umetsu et al. (2016) on the concentration–mass relation of massive clusters using combined strong lensing, weak lensing, and magnification measurements are fully consistent with the Diemer & Kravtsov (2015) relation, which we use as a basis to estimate the mean concentration for a general cluster population as function of mass and redshift. Meneghetti et al. (2014) found a higher average concentration for simulated clusters with regular X-ray morphologies resembling a subset of the CLASH clusters, similar to the results from Neto et al. (2007) for relaxed haloes. While most CLASH clusters are at significantly lower redshifts compared to RCS2 J2327, limiting a direct comparison, there are two CLASH clusters with a similar or higher redshift (MACS J0744+39 and CL J1226+3332). For these clusters Merten et al. (2015) estimated concentrations $c_{200c} = 4.1 \pm 1.0$ and $c_{200c} = 4.0 \pm 0.9$, respectively, in reasonable agreement with the simulation-based priors assumed in our analysis.

For a pure lensing signal the 45 degrees-rotated cross-component, shown as the open circles in Fig. 12, should be consistent with zero. The measured signal appears to be slightly negative, with a significance at the 1.9σ level when all data points at $r > 1$ Mpc are considered. This could possibly indicate the presence of residual systematics, for example from incomplete PSF anisotropy correction, which is typically referred to as additive shape measurement bias. While our employed basic KSB+ implementation was among the methods with the lowest additive biases in the blind test analysis from Heymans et al. (2006), there are simplifying assumptions in the KSB+ approach that may break down for complex PSFs (e.g. Kaiser 2000). As a sensitivity test to investigate if this can have a significant impact on our analysis, we artificially doubled the level of the PSF anisotropy correction. This reduces the significance of the negative cross-component to 1.1σ, but has only a very minor +2.7% impact on the estimated cluster mass. Compared to the statistical uncertainty we conclude that possible PSF anisotropy residuals are therefore of no concern for our current study. Potential future investigations with larger samples will be able to test for possible residual systematics with a higher sensitivity. If detected, such analyses could revert to alternative shape estimation techniques, which do not rely on simplifying assumptions regarding the PSF (e.g. Melchior et al. 2011).

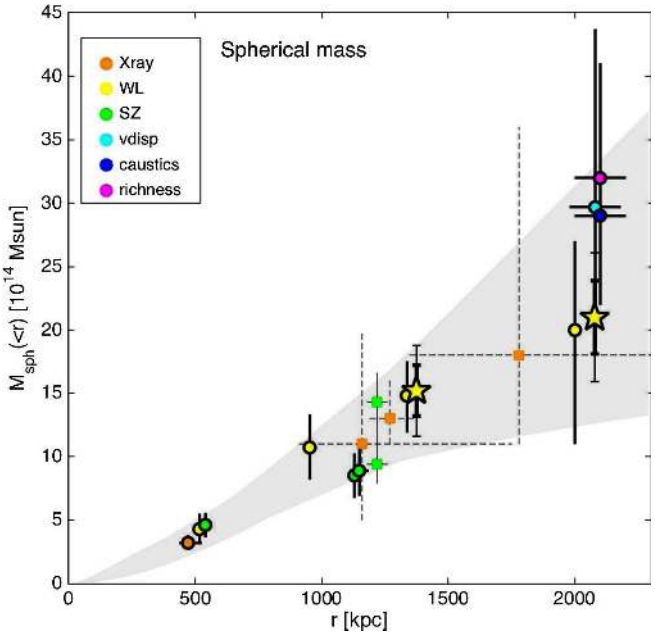

Fig. 13. Updated version of Fig. 16 from Sharon et al. (2015), showing various estimates for the enclosed spherical mass of RCS2 J2327 as function of radius. The stars-shaped data points show our weak lensing measurements, recomputed for $\Omega_m = 0.27$ and $\Omega_\Lambda = 0.73$ as assumed by Sharon et al. (2015). The thick (thin) error bars correspond to our combined statistical and systematic uncertainty without (with) including an additional ∼20% intrinsic scatter from cluster triaxiality and correlated large-scale structure. The green squares show SZ mass estimates from Hasselfield et al. (2013). The other mass measurements are described in Sharon et al. (2015) and were derived from Magellan spectroscopic, *Chandra* X-ray, SZA Sunyaev-Zel'dovich, and CFHT wide-field weak lensing observations, as well as richness measurements, where points with dashed error bars indicate extrapolated results. The shaded grey region shows the 1σ range of spherical NFW mass profiles Sharon et al. (2015) fit to the spherical mass estimates indicated with thick circles.

5.3. Comparison to results from previous studies

Sharon et al. (2015) presented a first weak lensing analysis of RCS2 J2327 based on deep wide-field CFHT/Megacam observations, yielding a mass constraint $M_{200c} = 2.0^{+0.9}_{-0.8} \times 10^{15}\ M_\odot$. Recomputing our analysis for the cosmology assumed in their study (ΛCDM with $\Omega_m = 0.27$, $\Omega_\Lambda = 0.73$, and $h = 0.7$), our result $M_{200c}/(10^{15}\ M_\odot) = 2.10^{+0.29}_{-0.27}(\text{stat.}) \pm 0.12(\text{sys.})$ is fully consistent with this previous measurement, but provides a constraint that is three times tighter. The major increase in sensitivity is also visible in Fig. 12, where the estimated tangential reduced shear profiles of the two studies scaled to the same $\langle\beta\rangle$ are

compared. While the CFHT results are noisier, they agree well for scales 1 Mpc $\lesssim r \lesssim$ 1.7 Mpc. However, at smaller radii the rescaled estimate from Sharon et al. (2015) is significantly lower than our estimated reduced shear profile. This may be a consequence of the colour selection scheme employed in Sharon et al. (2015), which yields only a partial removal of cluster galaxies and therefore needs to be complemented with a contamination correction, thereby introducing additional uncertainties especially at smaller radii. Sharon et al. (2015) also included measurements at larger radii, which are not probed by our HAWK-I observations.

We can also compare our weak lensing cluster mass constraints with mass estimates derived by Sharon et al. (2015) and Hasselfield et al. (2013) using other techniques. In particular, we compare to SZ and dynamical mass estimates, as they probe the cluster mass distribution at similar scales as the weak lensing signal. The dynamical mass constraints tend to be higher, for example $M_{200c}/(10^{15}\,M_\odot) = 2.9^{+1.0}_{-0.7}$ from a caustics analysis, but are still consistent with our measurements. There is a noticeable spread in the SZ-derived mass constraints for the cluster. Sharon et al. (2015) estimated a mass $M_{500c}/(10^{15}\,M_\odot) = 0.85 \pm 0.11$ based on scaling relations from Andersson et al. (2011) or $M_{500c}/(10^{15}\,M_\odot) = 0.89 \pm 0.08$ when employing the method from Mroczkowski (2011). Hasselfield et al. (2013) obtained a similar mass estimate $M_{500c}/(10^{15}\,M_\odot) = 0.94 \pm 0.15$ when assuming universal pressure profiles, but higher masses when assuming other scaling relations or models, for example $M_{500c}/(10^{15}\,M_\odot) = 1.49 \pm 0.30$ based on dynamical masses from Sifón et al. (2013). Our derived constraint $M_{500c}/(10^{15}\,M_\odot) = 1.52^{+0.19}_{-0.17}(\mathrm{stat.}) \pm 0.09(\mathrm{sys.})$, when assuming the same cosmology as Sharon et al. (2015), agrees well with the latter SZ results. We note that our mass constraint assumes a spherical NFW mass model. Cluster triaxiality and correlated large-scale structure can introduce an additional $\simeq$20% intrinsic scatter in comparison to the 3D halo mass (compare e.g. Becker & Kravtsov 2011). Likewise, there is intrinsic scatter between the 3D halo mass and SZ-inferred mass estimates. Figure 13 compares our results to the mass estimates from Sharon et al. (2015) and Hasselfield et al. (2013), where we show error bars for our constraints both with and without including intrinsic scatter.

Our analysis confirms that RCS2 $J2327$ is one of the most massive clusters known in the $z \gtrsim 0.7$ Universe. Its largest rival is likely ACT-CL $J0102{-}4915$ (Menanteau et al. 2012), for which existing weak lensing measurements indicate a possibly higher mass, but here the uncertainties are increased because of the complex merger geometry (compare S18; Jee et al. 2014). Comparing our improved mass constraints for RCS2 $J2327$ with the analysis from Buddendiek et al. (2015) we conclude that the existence of RCS2 $J2327$ does not pose a significant challenge to standard ΛCDM predictions.

6. Weak lensing performance: HAWK-I vs. ACS

A primary goal of this study is to investigate whether our experimental set-up, which employs shape measurements in high-resolution ground-based K_s images and a $g - z$ vs. $z - K_\mathrm{s}$ colour selection, can provide a viable alternative to mosaic HST observations for the weak lensing analysis of massive galaxy clusters at moderately high redshifts. For this we compare our results to the study from S18, as summarised in Table 1. In their work, S18 measured shapes in 2×2 ACS $F606W$ mosaics with single-orbit depth per pointing using the same underlying KSB+ implementation employed here. These authors applied a $V_{606} - I_{814} < 0.3$ colour selection (for clusters at $0.6 \lesssim z_\mathrm{l} \lesssim 1.0$). Here we consider only the case of adequately deep data for the colour selection as provided e.g. by the ACS $F814W$ imaging in S18. While the ACS background-selected source density is higher by a factor 1.85, this advantage is almost completely cancelled by the larger $\sigma_{\epsilon,\mathrm{eff}}$ and slightly lower $\langle\beta\rangle$ for the ACS catalogue (quoted numbers assume a cluster at $z_\mathrm{l} = 0.7$), yielding very similar weak lensing sensitivity factors f (see Eq. (8)) with $f_{\mathrm{HAWK-I}}/f_{\mathrm{ACS}} = 0.95$. Hence, our HAWK-I+LBC set-up provides a nearly identical weak lensing sensitivity as the ACS set-up employed by S18.

An important reason for the good performance of the HAWK-I+LBC set-up is given by the lower effective ellipticity dispersion $\sigma_{\epsilon,\mathrm{eff}}$ found for the colour-selected HAWK-I shear catalogue (see Sect. 4.8). In part this may be due to differences in the selected galaxy populations. But even for galaxies that would be included in both the HAWK-I and the ACS selection schemes we expect that the K_s-based shape measurements yield a lower intrinsic ellipticity dispersion as they primarily probe the smoother and typically rounder stellar component. In contrast, probing rest-frame UV wavelengths, the optical ACS imaging primarily shows clumpy star-forming regions, yielding more irregular shapes with a larger ellipticity dispersion. For illustration we compare the HAWK-I K_s images for some of the galaxies in our weak lensing catalogue to their counter parts in ACS $F814W$ images in Fig. 14. For example, the second but last galaxy shown in rows three and four exhibits a small light-emitting region in the ACS image likely constituting a compact star-forming region, which is spatially offset compared to the centre of the stellar light distribution visible in the K_s image.

In addition to the statistical performance we also have to compare the systematic uncertainties associated with both approaches, which is particularly relevant when considering future studies of larger samples. For this we ignore mass modelling uncertainties, as they are essentially identical for both approaches given the similar radial coverage, and given that they can be improved via simulations (e.g. see the discussion in S18). Residual shape measurement biases are in principle expected to be lower for the ACS-based analysis given the higher resolution (e.g. Massey et al. 2013). However, we expect that shape measurement biases will not be a limiting systematic for the analysis of future large weak lensing follow-up programmes of massive high-z clusters. Any such programme that is realistically conceivable in the next few years will have statistical uncertainties at the several per cent level, which is why systematic error control at the $\sim$1% level suffices (see also Köhlinger et al. 2015). With advanced shape measurement techniques, this level of accuracy has already been demonstrated for cosmic shear measurements (e.g. Fenech Conti et al. 2017), while Bernstein et al. (2016) even achieve a further order of magnitude improvement on simplified simulations. Additionally, Hoekstra et al. (2015, 2017) demonstrate how image simulations can be employed to calibrate shape measurement techniques for the impact of real survey effects for next generation cosmic shear experiments. What is currently still missing is the calibration of shape measurement algorithms in the stronger shear regime of clusters (see e.g. LSST Dark Energy Science Collaboration 2012), but such efforts are already well underway (e.g. Hernández-Martín et al., in prep.).

This leaves the final and most relevant source of systematic uncertainty, which is the calibration of the source redshift distribution and estimation of $\langle\beta\rangle$. Combining the various relevant contributors to this uncertainty in S18, the current systematic uncertainty on $\langle\beta\rangle$ amounts to $\sim$2.6% for the ACS-based

Table 1. Comparison of weak lensing data and performance.

	HAWK-I+LBC analysis	S18-like ACS analysis (with full-depth colour selection)
Shapes from (total duration)	VLT/HAWK-I K_s (≃7 h)	HST/ACS $F606W$ 2 × 2 mosaic (4 orbits ≃6.3 h)
For colours (total duration)	LBT/LBC $g + z$ (≃2 h)	HST/ACS $F814W$ mosaic (≃6.3 h) or 8m-class i band (≃2 h)[1]
Useful field of view	≃7′ × 7′	≃6.′5 × 6.′5
PSF FWHM	≃0.″35	≃0.″1
n_{gal}/arcmin^{-2}	9.8 (for $z_l \leq 1.1$)	18.1 (for $z_l \leq 1.0$)[2]
$\langle\beta\rangle(z_l = 0.7)$	0.481	0.466
$\sigma_{\epsilon,\mathrm{eff}}$	0.259	0.322
f/arcmin$^{-1}(z_l = 0.7)$	5.82	6.15

Notes. [(1)] This corresponds to the $F814W/i$-band imaging that would be needed to apply the colour selection for the full depth of the shape catalogue to reach the source density n_{gal}. [(2)] S18 reach this average source density for a colour selection including $F814W$ imaging and clusters at $z_l \leq 1.0$. At higher cluster redshifts a more stringent colour selection reduces the source density.

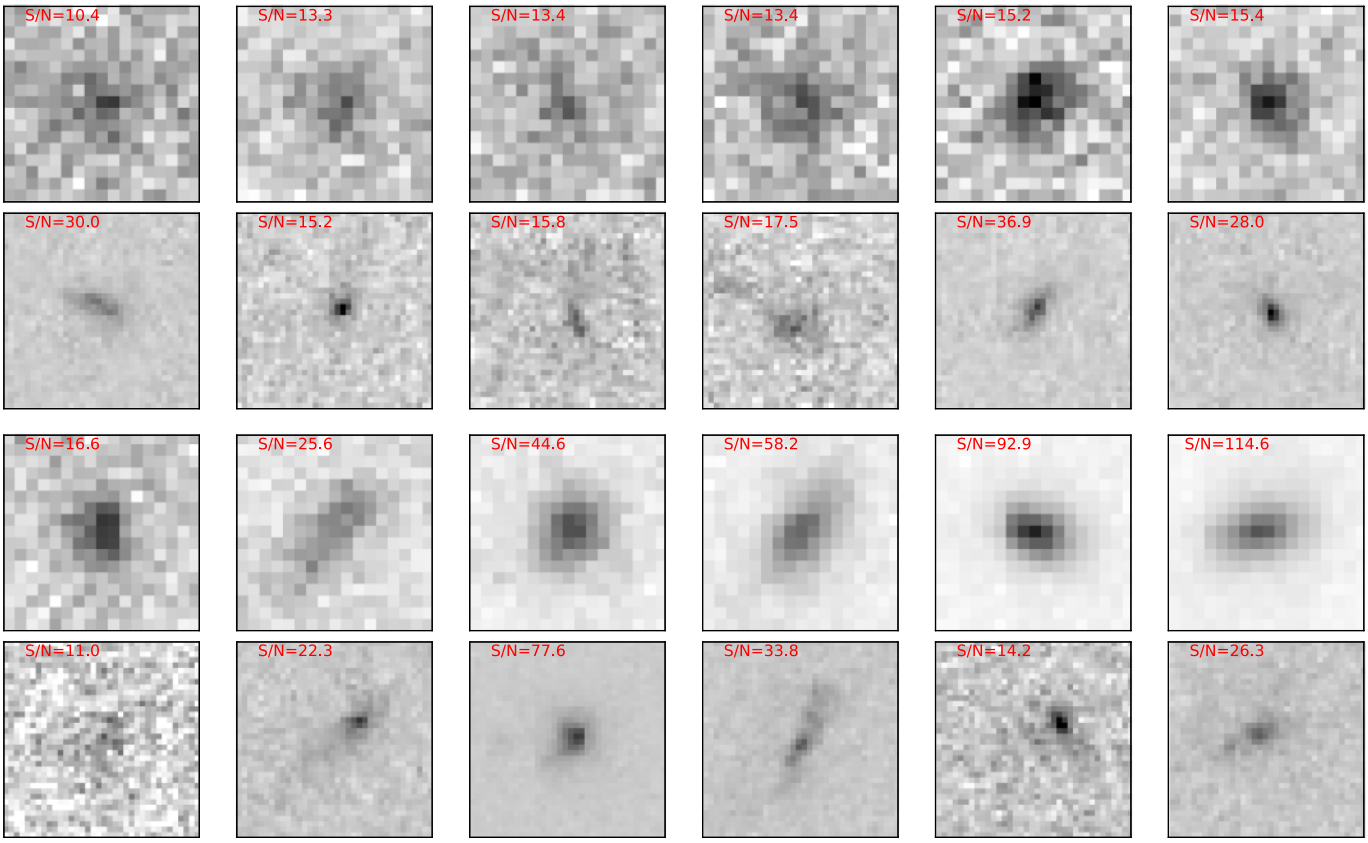

Fig. 14. 2.″0 × 2.″0 cut-outs of background-selected galaxies included in both the weak lensing catalogue obtained from the VLT/HAWK-I imaging and the weak lensing catalogue derived from the HST/ACS data. Rows one and three show the HAWK-I cut-outs sorted according to the HAWK-I $(S/N)_{flux}$, while rows two and four show the corresponding ACS cut-outs of the same galaxies. All cut-outs are oriented with north = up and east = left, and are centred on the HAWK-I galaxy position. The grey scale is linear with flux for all cut-outs, but the range in flux is adjusted according the individual $(S/N)_{flux}$.

analysis. For comparison, the systematic effects considered in Sect. 4.5.3 yield a smaller combined systematic uncertainty on $\langle\beta\rangle$ for the HAWK-I-based analysis of ∼0.7%. One of the reasons for this low systematic uncertainty is the availability of NIR-selected reference samples with deep high-quality redshift information. In particular in the 3D-HST reference sample effectively ∼71% of the colour-selected galaxies at the relevant depth have a spectroscopic or HST/WFC3 grism redshift when taking our source magnitude distribution and weights into account (see Sect. 4.3.2). Comparably deep and complete spectroscopic reference samples do not yet exist for the deep optically selected ACS weak lensing data sets (but samples are increasing, see e.g. Le Fèvre et al. 2015). In S18 a significant contribution to the systematic uncertainty related to the $\langle\beta\rangle$ estimate comes from the correction for catastrophic redshift outliers. These incorrectly scatter from the high-z source population into a low-z contamination sample, which cannot be removed with the colour selection scheme from S18. The gzK_s selection applied in our current study does not suffer from such a low-z contamination, and is therefore affected less by catastrophic redshift outliers.

There are further advantages of the HAWK-I+LBC-based analysis. The chosen default colour selection scheme can be

applied out to a higher maximum cluster redshift $z_{\rm l,max} = 1.1$ (instead of $z_{\rm l} = 1.0$ for the $V_{606} - I_{814} < 0.3$ ACS colour selection scheme), which can possibly be extended to $z_{\rm l,max} \simeq 1.2$–1.3 (instead of $z_{\rm l} = 1.15$ for the ACS-based analysis) with more stringent colour selection criteria (compare Figs. 5 and 6). The HAWK-I+LBC-based colour selection also yields a better suppression fraction of galaxies at relevant cluster redshifts (98.9% vs. 98.1%).

Taking all this together we conclude that the chosen set-up of the HAWK-I+LBC data yields a weak lensing performance that is similarly powerful as the considered ACS-based analysis scheme. While the required integration time is significant for the $K_{\rm s}$ imaging, this is compensated by the ability to cover a larger field of view with imagers such as HAWK-I. The $K_{\rm s}$-based approach is therefore particularly efficient for the analysis of high-mass ($M_{\rm 200c} > 5 \times 10^{14}\ M_{\odot}$) clusters at redshifts $0.7 \lesssim z_{\rm l} \lesssim 1.1$, for which mosaics would be needed with HST/ACS to probe the weak lensing signal out to approximately the virial radius[9] (see Table 1 for the approximate total observing times). For less massive clusters and clusters at even higher redshifts deeper observations are needed, while a wide angular coverage is less important (e.g. Jee et al. 2011). In this regime deeper single pointing HST observations likely provide a more adequate observing strategy, as required $K_{\rm s}$ integration times would become prohibitively long, and the virial radius fits within the ACS field of view.

7. Summary and conclusions

We have presented the first weak gravitational lensing analysis that exploits the superb image resolution ($FWHM^{*} = 0\farcs35$) that can be achieved in the $K_{\rm s}$ band under good seeing conditions with optimised imagers such as the employed VLT/HAWK-I to measure weak lensing galaxy shapes. Here we summarise our main conclusions:

- At the resolution of the $K_{\rm s}$ imaging, nearly all relevant background galaxies are sufficiently resolved for weak lensing measurements.
- The employed photometric selection in $g - z$ vs. $z - K_{\rm s}$ colour space is highly effective for the selection of most of the lensed background galaxies and the removal of diluting foreground and cluster galaxies.
- Our analysis indicates that the intrinsic ellipticity dispersion is noticeably lower for high-z galaxies in $K_{\rm s}$ weak lensing data compared to high-z sources studied in the optical, boosting the weak lensing sensitivity.
- Despite a lower source density the analysed data therefore yield almost the same weak lensing sensitivity as the analysis of mosaic HST/ACS data with single-orbit depth per pointing from S18.
- The systematic uncertainty regarding the calibration of the source redshift distribution is lower for the HAWK-I analysis compared to the S18 ACS analysis. This is thanks to the use of NIR-selected redshift reference samples from 3D-HST and UltraVISTA and the improved removal of contaminating low-z galaxies from the source sample, reducing the sensitivity to catastrophic redshift errors.
- Comparing to HST/ACS data that overlap with parts of our HAWK-I observations of RCS2 $J2327$, we find fully consistent estimates of the tangential reduced shear profile between the two data sets in a matched catalogue, providing an important confirmation for the $K_{\rm s}$-based analysis.
- Given the larger field of view, good-seeing VLT/HAWK-I $K_{\rm s}$ observations, complemented with g and z (or B and z) photometry, provide an efficient alternative to mosaic HST/ACS observations for the weak lensing analysis of massive galaxy clusters at redshifts $0.7 \lesssim z_{\rm l} \lesssim 1.1$.
- Especially for clusters at higher redshifts significantly deeper observations with higher resolution are required, while a smaller field of view is typically sufficient. In this regime deep HST observations with a smaller angular coverage provide the most effective and efficient observing strategy.
- We stress that calibrations of the source redshift distribution for weak lensing studies have to carefully account for catastrophic redshift outliers, which appear to be present even when NIR imaging is available (see Sect. 4.3.3).
- While our observations confirm that RCS2 $J2327$ is one of the most massive galaxy clusters known in the $z \gtrsim 0.7$ Universe, its existence is not in tension with standard ΛCDM expectations according to our mass constraints.
- The extreme mass of RCS2 $J2327$ leads to the significant weak lensing signal we detect, but we stress that our conclusions regarding the sensitivity of the HAWK-I weak lensing measurements (hence, the noise level) do not depend on its extreme mass. The approach is also directly applicable to massive, but less extreme clusters at redshifts $0.7 \lesssim z_{\rm l} \lesssim 1.1$ (e.g. from the Bleem et al. 2015 sample).

Acknowledgements. This work is directly based on observations collected at the European Organisation for Astronomical Research in the Southern Hemisphere under ESO programme(s) 087.A-0933, at the Large Binocular Telescope (LBT), and with the NASA/ESA *Hubble* Space Telescope under GO programmes 13177 and 10846. This work also makes use of catalogues created by the 3D-HST Treasury Program (GO 12177 and 12328) and catalogues derived from the ESO UltraVISTA Programme 179.A-2005. We thank ESO staff for obtaining the excellent VLT/HAWK-I images and Paul Martini, David Atlee, Erica Hesselbach, Jeff Blackburne, and Matthias Dietrich for conducting the LBT/LBC observations. We thank Patrick Simon for providing the codes employed in this work to reconstruct the cluster mass distribution and to generate Gaussian shear field realisations for the estimation of the impact of large-scale structure projections. We thank Peter Schneider for useful discussions and for providing comments on this manuscript. TS, DA, BH, and DK acknowledge support from the German Federal Ministry of Economics and Technology (BMWi) provided through DLR under projects 50 OR 1210, 50 OR 1308, 50 OR 1407, and 50 OR 1610. RFJvdB acknowledges support from the European Research Council under FP7 grant number 340519. TE is supported by the Deutsche Forschungsgemeinschaft in the framework of the TR33 "The Dark Universe". HHi is supported by an Emmy Noether grant (No. Hi 1495/2-1) of the Deutsche Forschungsgemeinschaft. This work was supported in part by the Kavli Institute for Cosmological Physics at the University of Chicago through grant NSF PHY-1125897 and an endowment from the Kavli Foundation and its founder Fred Kavli. Part of the research was carried out at the Jet Propulsion Laboratory, California Institute of Technology, under a contract with the National Aeronautics and Space Administration. HST is operated by the Association of Universities for Research in Astronomy, Incorporated, under NASA contract NAS5-26555. The LBT is an international collaboration among institutions in the United States, Italy and Germany. LBT Corporation partners are The University of Arizona on behalf of the Arizona university system; Istituto Nazionale di Astrofisica, Italy; LBT Beteiligungsgesellschaft, Germany, representing the Max-Planck Society, the Astrophysical Institute Potsdam, and Heidelberg University; The Ohio State University, and The Research Corporation, on behalf of The University of Notre Dame, University of Minnesota and University of Virginia. This research made use of APLpy, an open-source plotting package for Python (Robitaille & Bressert 2012).

[9] The achievable signal-to-noise ratio of the mass constraints naturally increases with cluster mass and decreases with cluster redshift. For example, for an individual $M_{\rm 200c} \simeq 6 \times 10^{14}\ M_{\odot}$ cluster at $z \simeq 1.0$ and a set-up similar to our analysis we expect a ~50% statistical mass uncertainty.

References

Andersson, K., Benson, B. A., Ade, P. A. R., et al. 2011, ApJ, 738, 48
Bartelmann, M., & Schneider, P. 2001, Phys. Rep., 340, 291
Becker, M. R., & Kravtsov, A. V. 2011, ApJ, 740, 25

Bernstein, G. M., Armstrong, R., Krawiec, C., & March, M. C. 2016, MNRAS, 459, 4467
Bertin, E. 2006, in Astronomical Data Analysis Software and Systems XV, eds. C. Gabriel, C. Arviset, D. Ponz, & S. Enrique, ASP Conf. Ser., 351, 112
Bertin, E. 2011, in Astronomical Data Analysis Software and Systems XX, eds. I. N. Evans, A. Accomazzi, D. J. Mink, & A. H. Rots, ASP Conf. Ser., 442, 435
Bertin, E., & Arnouts, S. 1996, A&AS, 117, 393
Bertin, E., Mellier, Y., Radovich, M., et al. 2002, in Astronomical Data Analysis Software and Systems XI, ed. D. A. Bohlender, D. Durand, & T. H. Handley, ASP Conf. Ser., 281, 228
Bleem, L. E., Stalder, B., de Haan, T., et al. 2015, ApJS, 216, 27
Bradač, M., Ryan, R., Casertano, S., et al. 2014, ApJ, 785, 108
Broadhurst, T. J., Taylor, A. N., & Peacock, J. A. 1995, ApJ, 438, 49
Buddendiek, A., Schrabback, T., Greer, C. H., et al. 2015, MNRAS, 450, 4248
Daddi, E., Cimatti, A., Renzini, A., et al. 2004, ApJ, 617, 746
Diemer, B., & Kravtsov, A. V. 2015, ApJ, 799, 108
Dietrich, J. P., Böhnert, A., Lombardi, M., Hilbert, S., & Hartlap, J. 2012, MNRAS, 419, 3547
Erben, T., Van Waerbeke, L., Bertin, E., Mellier, Y., & Schneider, P. 2001, A&A, 366, 717
Erben, T., Schirmer, M., Dietrich, J. P., et al. 2005, Astron. Nachr., 326, 432
Fenech Conti, I., Herbonnet, R., Hoekstra, H., et al. 2017, MNRAS, 467, 1627
Fort, B., Mellier, Y., & Dantel-Fort, M. 1997, A&A, 321, 353
Giallongo, E., Ragazzoni, R., Grazian, A., et al. 2008, A&A, 482, 349
Gilbank, D. G., Gladders, M. D., Yee, H. K. C., & Hsieh, B. C. 2011, AJ, 141, 94
Grogin, N. A., Kocevski, D. D., Faber, S. M., et al. 2011, ApJS, 197, 35
Hasselfield, M., Hilton, M., Marriage, T. A., et al. 2013, J. Cosmol. Astropart. Phys., 7, 8
Heymans, C., Van Waerbeke, L., Bacon, D., et al. 2006, MNRAS, 368, 1323
Hinshaw, G., Larson, D., Komatsu, E., et al. 2013, ApJS, 208, 19
Hoag, A., Bradač, M., Huang, K. H., et al. 2015, ApJ, 813, 37
Hoekstra, H., Franx, M., Kuijken, K., & Squires, G. 1998, ApJ, 504, 636
Hoekstra, H., Franx, M., & Kuijken, K. 2000, ApJ, 532, 88
Hoekstra, H., Bartelmann, M., Dahle, H., et al. 2013, Space Sci. Rev., 177, 75
Hoekstra, H., Herbonnet, R., Muzzin, A., et al. 2015, MNRAS, 449, 685
Hoekstra, H., Viola, M., & Herbonnet, R. 2017, MNRAS, 468, 3295
Jarvis, M., & Jain, B. 2004, ArXiv e-prints [arXiv:astro-ph/0412234]
Jee, M. J., Blakeslee, J. P., Sirianni, M., et al. 2007, PASP, 119, 1403
Jee, M. J., Rosati, P., Ford, H. C., et al. 2009, ApJ, 704, 672
Jee, M. J., Dawson, K. S., Hoekstra, H., et al. 2011, ApJ, 737, 59
Jee, M. J., Hughes, J. P., Menanteau, F., et al. 2014, ApJ, 785, 20
Kaiser, N. 2000, ApJ, 537, 555
Kaiser, N., & Squires, G. 1993, ApJ, 404, 441
Kaiser, N., Squires, G., & Broadhurst, T. 1995, ApJ, 449, 460
King, L. J., Clowe, D. I., Lidman, C., et al. 2002, A&A, 385, L5
Kissler-Patig, M., Pirard, J.-F., Casali, M., et al. 2008, A&A, 491, 941
Koekemoer, A. M., Fruchter, A. S., Hook, R. N., & Hack, W. 2003, in HST Calibration Workshop : Hubble after the Installation of the ACS and the NICMOS Cooling System, eds. S. Arribas, A. Koekemoer, & B. Whitmore, 337
Koekemoer, A. M., Faber, S. M., Ferguson, H. C., et al. 2011, ApJS, 197, 36
Köhlinger, F., Hoekstra, H., & Eriksen, M. 2015, MNRAS, 453, 3107
Kuijken, K., Heymans, C., Hildebrandt, H., et al. 2015, MNRAS, 454, 3500
Le Fèvre, O., Tasca, L. A. M., Cassata, P., et al. 2015, A&A, 576, A79
Leauthaud, A., Massey, R., Kneib, J.-P., et al. 2007, ApJS, 172, 219
Leauthaud, A., Tinker, J., Bundy, K., et al. 2012, ApJ, 744, 159
LSST Dark Energy Science Collaboration. 2012, ArXiv e-prints [arXiv:1211.0310]
Luppino, G. A., & Kaiser, N. 1997, ApJ, 475, 20
Mandelbaum, R., Miyatake, H., Hamana, T., et al. 2018, PASJ, 70, S25
Martinez, P., Kolb, J., Tokovinin, A., & Sarazin, M. 2010, A&A, 516, A90
Massey, R., Rhodes, J., Leauthaud, A., et al. 2007, ApJS, 172, 239
Massey, R., Hoekstra, H., Kitching, T., et al. 2013, MNRAS, 429, 661
Massey, R., Schrabback, T., Cordes, O., et al. 2014, MNRAS, 439, 887
Masters, D. C., Stern, D. K., Cohen, J. G., et al. 2017, ApJ, 841, 111
Mayen, C., & Soucail, G. 2000, A&A, 361, 415
McCracken, H. J., Milvang-Jensen, B., Dunlop, J., et al. 2012, A&A, 544, A156
McInnes, R. N., Menanteau, F., Heavens, A. F., et al. 2009, MNRAS, 399, L84
Melchior, P., Viola, M., Schäfer, B. M., & Bartelmann, M. 2011, MNRAS, 412, 1552
Menanteau, F., Hughes, J. P., Sifón, C., et al. 2012, ApJ, 748, 7
Menanteau, F., Sifón, C., Barrientos, L. F., et al. 2013, ApJ, 765, 67
Meneghetti, M., Rasia, E., Vega, J., et al. 2014, ApJ, 797, 34
Merten, J., Meneghetti, M., Postman, M., et al. 2015, ApJ, 806, 4
Momcheva, I. G., Brammer, G. B., van Dokkum, P. G., et al. 2016, ApJS, 225, 27
Mroczkowski, T. 2011, ApJ, 728, L35
Muzzin, A., Marchesini, D., Stefanon, M., et al. 2013, ApJS, 206, 8
Navarro, J. F., Frenk, C. S., & White, S. D. M. 1997, ApJ, 490, 493
Neto, A. F., Gao, L., Bett, P., et al. 2007, MNRAS, 381, 1450
Planck Collaboration XIII. 2016, A&A, 594, A13
Postman, M., Coe, D., Benítez, N., et al. 2012, ApJS, 199, 25
Robitaille, T., & Bressert, E. 2012, APLpy: Astronomical Plotting Library in Python, Astrophysics Source Code Library
Rowe, B. T. P., Jarvis, M., Mandelbaum, R., et al. 2015, Astron. Comput., 10, 121
Schirmer, M. 2013, ApJS, 209, 21
Schneider, P., & Seitz, C. 1995, A&A, 294, 411
Schrabback, T., Erben, T., Simon, P., et al. 2007, A&A, 468, 823
Schrabback, T., Hartlap, J., Joachimi, B., et al. 2010, A&A, 516, A63
Schrabback, T., Applegate, D., Dietrich, J. P., et al. 2018, MNRAS, 474, 2635
Scoville, N., Aussel, H., Brusa, M., et al. 2007, ApJS, 172, 1
Seitz, S., & Schneider, P. 1996, A&A, 305, 383
Seitz, C., & Schneider, P. 1997, A&A, 318, 687
Sharon, K., Gladders, M. D., Marrone, D. P., et al. 2015, ApJ, 814, 21
Sifón, C., Menanteau, F., Hasselfield, M., et al. 2013, ApJ, 772, 25
Simon, P., Taylor, A. N., & Hartlap, J. 2009, MNRAS, 399, 48
Skelton, R. E., Whitaker, K. E., Momcheva, I. G., et al. 2014, ApJS, 214, 24
Skrutskie, M. F., Cutri, R. M., Stiening, R., et al. 2006, AJ, 131, 1163
Thölken, S., Schrabback, T., Reiprich, T. H., et al. 2018, A&A, 610, A71
Umetsu, K., Zitrin, A., Gruen, D., et al. 2016, ApJ, 821, 116
Viola, M., Kitching, T. D., & Joachimi, B. 2014, MNRAS, 439, 1909
von der Linden, A., Allen, M. T., Applegate, D. E., et al. 2014, MNRAS, 439, 2
Wright, C. O., & Brainerd, T. G. 2000, ApJ, 534, 34